A Martian General Circulation Experiment with Large Topography[1]

JAMES B. POLLACK

NASA Ames Research Center, Mountain View, CA 94035

CONWAY B. LEOVY

Department of Atmospheric Sciences, University of Washington, Seattle 98195

PAUL W. GREIMAN

Department of Meteorology, Florida State University, Tallahassee 32306

YALE MINTZ

Laboratory for Atmospheric Sciences, NASA Goddard Space Flight Center, Greenbelt, MD 20771

(Manuscript received 7 January 1980, in final form 7 July 1980)

ABSTRACT

A three-layer general circulation model, used to simulate the Martian atmosphere, is described and results are presented. The model assumes a dust-free pure CO_2 atmosphere and allows for a diurnally-varying convective boundary layer. Smoothed Martian topography and albedo variations are incorporated. The simulation described is for the period near southern winter solstice, season of the Viking landings. The zonally-averaged circulation, mass, heat and momentum balances, and properties of stationary and transient waves are described in some detail, and are compared with results of previous simulations of the Martian general circulation, with related features of the Earth's general circulation, and with observed characteristics of the Martian atmosphere.

The principal conclusions are the following: 1) The simulated zonally-averaged circulation is not very sensitive to differences between this model and the earlier general circulation model of Leovy and Mintz (1969), and compares reasonably well with observations, except for differences attributable to dust and season. 2) The meridional mass flow produced by the seasonal condensation of CO_2 in the winter polar region has a major influence on the circulation, but, because of the weak influence of atmospheric heat transport, it is controlled almost entirely by radiation. 3) Quasi-barotropic stationary waves, forced kinematically by the topography and resembling topographically-forced terrestrial planetary waves, are generated by the model in the winter hemisphere region of strong eastward flow, while baroclinic stationary waves are thermally forced by topography in the tropics and summer subtropics. 4) Transient baroclinically unstable waves, of somewhat lower dominant wavenumber than those found on the Earth, are generated in winter midlatitudes and their amplitudes, wavenumbers and phase speeds closely agree with what has been deduced from the Viking lander observations.

1. Introduction

An earlier simulation of the Martian atmospheric general circulation employed a two-level version of the UCLA primitive equation model modified to apply to Mars, but with the lower boundary taken to be a level surface (Leovy and Mintz, 1969; henceforth Paper I). Two seasons were simulated: southern summer solstice and southern autumn equinox. In the solstice experiment, the results showed a broad and intense thermally direct Hadley circulation, eastward traveling wave cyclones at high latitudes of the winter hemisphere and strong diurnal tides in the tropics and summer hemisphere. The traveling waves, though strong by terrestrial standards, did not transport enough heat into the winter polar cap region to significantly influence the rate of CO_2 condensation on the surface polar cap which was therefore governed almost entirely by the net radiation from the surface. The rate of condensation on the cap was significant for the circulation dynamics because it produced a substantial net meridional mass flow and meridional transport of angular momentum.

In the present study, two major shortcomings of that simulation have been corrected: the very large-amplitude large-scale topography which is now known to exist on Mars has been incorporated

[1] Contribution No. 561, Department of Atmospheric Sciences, University of Washington.

0022-4928/81/010003-27$10.75

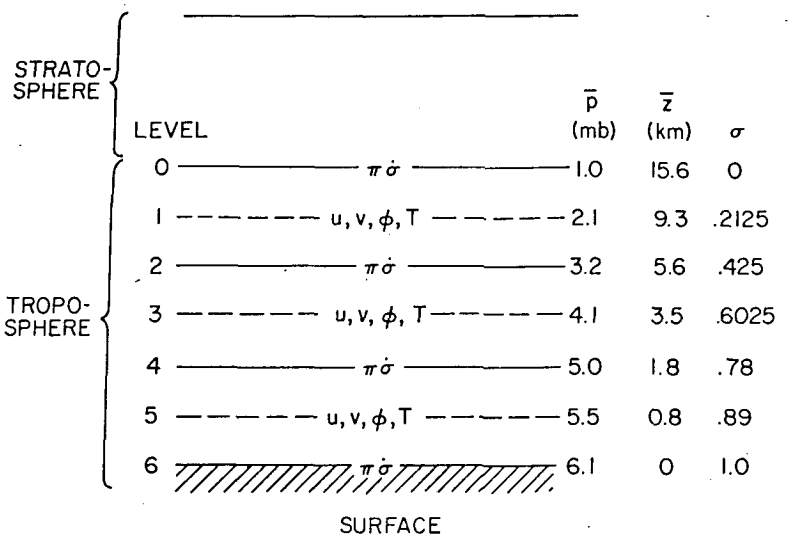

FIG. 1. σ-coordinate structure of the model with level mean pressures and altitudes.

into the model, and a third model layer has been added, primarily to allow a more accurate simulation of the strong diurnal variations of temperature and wind in the planetary boundary layer. In addition, improvements have been made in the radiative and convective heating algorithms and the frictional algorithm, in the space finite-differencing scheme, and in the horizontal resolution. The present simulation is for the period around southern winter solstice, the season of the Viking spacecraft landings, but was done before the landings took place. Consequently, suspended atmospheric dust, which is now known to make an important radiative contribution to atmospheric and surface heating (Pollack *et al.*, 1977, 1979) was not incorporated in the model. Nevertheless, the results reported here should provide a useful basis for comparison with subsequent simulations in which dust is included.

This paper describes the principal features of the model physics (with details relegated to an Appendix), and the results are presented and discussed with emphasis on the following issues: similarities and differences in the simulated circulation with respect to changes in the model from that of Paper I, especially differences attributable to topography, similarities and differences between the simulation results and available spacecraft observations,[2] and similarities and differences between the large-scale dynamical processes in the atmospheres of the Earth and Mars.

2. Model

A version of the UCLA primitive equation general circulation model (Arakawa, 1972)[3] was adapted for the Martian calculation. This version of the UCLA model was also the prototype for models which were developed and applied successfully to the Earth's atmosphere at the NASA Goddard Institute for Space Studies (the GISS model; Somerville *et al.*, 1974; Stone *et al.*, 1977), and at the Goddard Space Flight Center (the GLAS model; Halem *et al.*, 1979). Our changes involved the external parameters appropriate to Mars, different algorithms for calculating atmospheric and surface heating and friction, and addition of an algorithm to account for the condensation of the major atmospheric constitution CO_2 at the surface.

a. Basic equations and grid arrangement

The model employs the primitive equations in a three-level σ-coordinate system with fixed tropopause pressure, $p_T = 1.0$ mb, at the $\sigma = 0$ level. As in Paper I, the "stratosphere" above this level was assumed to be dynamically inert, but was taken into account in calculating radiative heating. Fig. 1 illustrates the vertical arrangement of the grid.

The prognostic variables (horizontal velocity components, u, v; temperature T; and the surface pressure variable $\pi \equiv p_s - p_T$) were evaluated on the staggered finite-difference grid of Arakawa (the

[2] Some preliminary results of this experiment, emphasizing winds at the Viking lander sites at the season of landing, were reported at the time of the Viking landings (Pollack *et al.*, 1976).

[3] Arakawa, A., 1972: *Design of the UCLA general circulation model*. Tech. Rep. No. 7, Numerical Simulations of Weather and Climate. Dept. of Meteorology, University of California, Los Angeles, 116 pp.

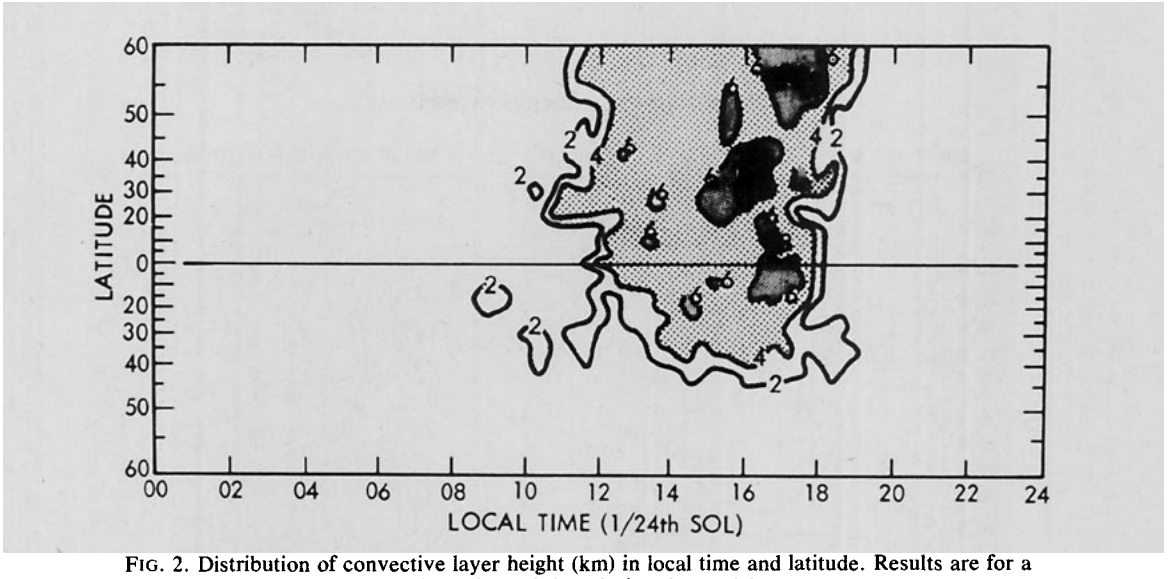

FIG. 2. Distribution of convective layer height (km) in local time and latitude. Results are for a particular universal time during the model run.

"Arakawa C-scheme"), using a latitude-longitude grid with 37 intervals (5° spacing) in latitude and 60 intervals (6° spacing) in longitude. The geopotential Φ, a diagnostic variable, was obtained from the hydrostatic equation and the prescribed surface elevation, Φ_s. The σ-vertical velocity $\dot{\sigma}$ was obtained from the mass continuity equation and the boundary conditions, $\dot{\sigma} = 0$ at $\sigma = 0$, and $\dot{\sigma}$ equal to the rate of condensation or sublimation of CO_2 at $\sigma = 1$ (see Subsection 2d). The time-marching scheme of Arakawa (1972)[3] was used with a time step of 277.422 s, 20% smaller than the longest that could be used without linear computational instability, determined by trial and error. Fourier smoothing in longitude was employed at latitudes $> 45°$ to insure linear computational stability despite the convergence of the meridians in high latitudes. The time step was compatible with the Martian solar day, or "sol" (88775 s): 1 time step = 1/320 sol. To save computation time, the heating and friction were calculated every fifth time step. The heating and friction algorithms are described briefly below, and their details are given in the Appendix.

b. *Heating algorithms*

The contributions of solar radiation, thermal infrared radiation, and vertical convective heat exchange to the total diabatic heating were calculated at each grid point. Carbon dioxide was assumed to be the only atmospheric gaseous constituent. The small amounts of ^{40}A and N_2 which are present are radiatively and dynamically unimportant (Owen and Biemann, 1976). Trace amounts of water vapor are present in the warmer regions and can play a radiative role, but rough calculations indicate that the water vapor contribution to the total heating rate is normally very small and it was neglected. Under exceptional circumstances, ozone can contribute significantly to heating of the Martian atmosphere (Kuhn *et al.*, 1979) but it was neglected also. Atmospheric aerosols, including dust, were neglected except for the radiative effects of the winter season "polar hood" clouds which were assumed to consist of water ice particles. These were crudely accounted for using a prescribed distribution of cloudiness.

Absorption of solar radiation by CO_2 in the near IR bands (1.3, 1.4, 1.6, 2.0, 2.7 and 4.3 μm) was calculated, using functional expressions for the dependence of their equivalent widths on absorber mass, pressure and temperature based on laboratory data. Thermal infrared radiative exchange by the 15 μm band of CO_2 was also treated using an expression for the whole band equivalent width based on the same data.

The polar hood water ice cloud was assumed to contribute to the total planetary albedo A at each grid point where cloud occurred according to

$$A = A_c + (1 - A_c)^2 A_s/(1 - A_c A_s), \qquad (1)$$

where A_s is surface albedo, and A_c, the cloud albedo, was assumed to have the constant value 0.124. A constant infrared emissivity was also assigned to these clouds and was distributed over the two lowest model layers in proportion to the mass of each layer. The value of this emissivity was derived from the single-scattering albedo, asymmetry parameter, and ratio of infrared to visible optical depths for a size distribution of spherical ice particles having a cross section mean radius of 2 μm, as suggested by the

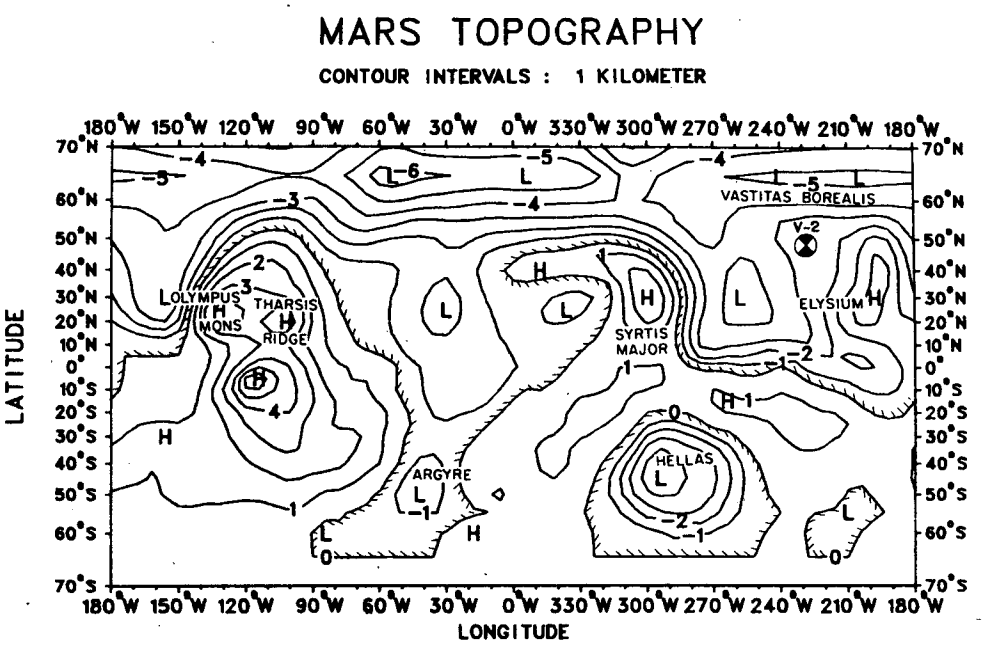

FIG. 3. Latitude-longitude distribution of topography. Contour interval 1 km.

analysis of Curran *et al.* (1973). Mie calculations and the optical constants of water ice (Irvine and Pollack, 1968) were used to evaluate these single-scattering parameters. The effect of multiple scattering on the emissivity was accounted for crudely with the aid of the two-stream approximation of Sagan and Pollack (1967).

Water ice cloud was prescribed to occur exclusively over the winter polar region at latitudes south of 40°S. This distribution was based largely on generally accepted interpretations of telescopic observations (Slipher, 1962), and on Mariner 9 observations of the winter North Polar hood (Briggs and Leovy, 1974), but it is now known that the South Polar region is relatively free of water ice clouds during mid-winter (Briggs *et al.*, 1979), so that this prescribed coverage may have been too extensive. The polar hood ice clouds, however, probably had very little influence on our simulation results, because the contributions of the clouds to the net infrared and solar flux densities at the surface were individually small. Moreover, these fluxes tended to compensate each other in the partially sunlit region, between 40°S and the polar night boundary, and the influence of the clouds on the total column heat balance (ground plus atmosphere) was small in all of the polar hood latitudes.

Convective heating was calculated using an energy conserving convective adjustment to the Martian dry adiabatic lapse rate, and an algorithm for conductive-convective heat transfer across the ground-atmosphere interface based on empirical studies of the Earth's planetary boundary layer (Deardorff, 1972). The stability of the surface layer was determined by comparing the ground surface temperature with the extrapolated atmospheric surface temperature. When the surface boundary layer was stable, convective heat exchange involved the lowest model layer only. When it was unstable, the convective heat flux convergence was evaluated for each layer, assuming that the heat flux decreased linearly with pressure from its value at the ground to a value of zero at the top of a convective layer. The height and potential temperature of the convective layer were determined diagnostically from the potential temperatures of the layers, the extrapolated surface atmospheric potential temperature, and the interpolated potential temperatures at the layer interfaces by a procedure described in the Appendix. The convective layer was not confined to the lowest model layer but was allowed to extend upward as far as the model tropopause. This procedure produced a realistic diurnally varying boundary layer (Fig. 2).

c. Frictional algorithms

The rationale governing the modeling of both convective heat transport and friction was that the algorithms employed should depend as little as possible on ad hoc parameterizations of poorly understood processes. Consequently, only two frictional processes were modeled explicitly (aside from the small damping implicit in the finite difference scheme). Surface stress, applied to the lowest

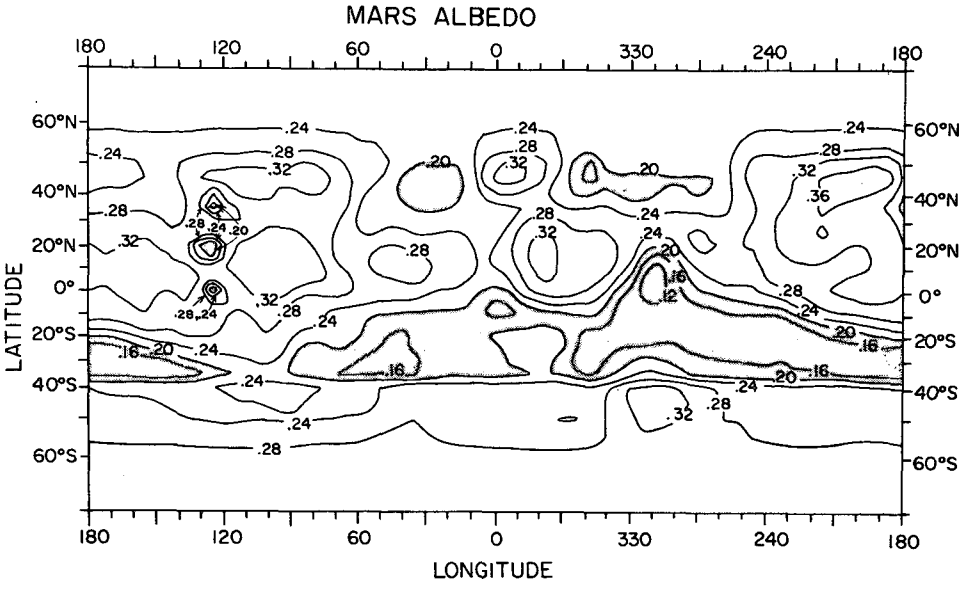

FIG. 4. Latitude-longitude distribution of surface albedo. Contour interval 0.04.

layer, was modeled using a stability dependent prescription for the surface drag coefficient, based on terrestrial planetary boundary-layer experience (Deardorff, 1972). Under stable surface-layer conditions, the stress of the atmosphere on the ground was assumed to act at a fixed angle of 30° to the direction of the lowest layer wind with the stress component perpendicular to the wind always directed toward lower pressure. Under unstable conditions, stress acted in the same direction as the lowest layer wind.

In addition, Richardson number adjustment, a momentum conserving redistribution of momentum between two layers, occurred whenever the Richardson number, defined in terms of the potential temperatures at the layer mean pressure levels and the layer mean winds, fell below the critical value of 1.0. Whenever convective adjustment occurred, an instantaneous Richardson number adjustment was made in such a way as to equalize the wind in each of the convectively-adjusted layers. It turned out that Richardson number adjustment occurred most frequently in conjunction with convective adjustment. Whenever the Richardson number was below 1.0, but the layers were convectively stable, layer winds were relaxed to the critical Richardson number with an adjustment time of 2×10^4 s.

d. *Ground temperature and CO_2 phase change*

Ground temperature variations, including the diurnal variations, were calculated using an algorithm similar to that used in Paper I. When the ground temperature T_G exceeded the frost point temperature of CO_2, the heat balance equation was applied at $\sigma = 1$:

$$\sigma T_G^4 - F_{IR}^{\downarrow} - (1 - A)F_s + F_{conv} + F_{cond} = 0, \quad (2)$$

where σ is the Stefan-Boltzmann constant, $F_{IR}^{\downarrow}$ the downward thermal infrared flux, F_s the downward solar flux, F_{conv} the (upward) convective heat flux, and F_{cond} the (downward) conductive heat flux. In order to obtain a convenient explicit time-dependent expression for T_G, F_{cond} was approximated by

$$F_{cond} = (2\omega)^{-1/2} I \left[\frac{\partial T_G}{\partial t} + \omega(T_G - T_\infty) \right], \quad (3)$$

where I is the thermal inertia of the soil, ω the diurnal frequency and T_G a smoothly varying "deep temperature" [see Paper I for further discussion of Eq. (3)]. The value of I was obtained from analyses of observations of the diurnal temperature variations (Kieffer *et al.*, 1973), and was assumed to be uniform over the entire planet. The deep temperature was set equal to the running average of T_G over the preceding 0.2 sol. This averaging time was chosen to give the best overall agreement between ground temperatures evaluated by the approximate formulas [Eqs. (2) and (3)] and published curves for which the conductive heat flux was evaluated more exactly (Gierasch and Goody, 1968).

Although atmospheric heating and friction were computed only every fifth time step, changes in T_G and in its most rapidly varying driver, $(1 - A)F_s$, were computed every time step.

The condensation temperature of CO_2 was approximated as

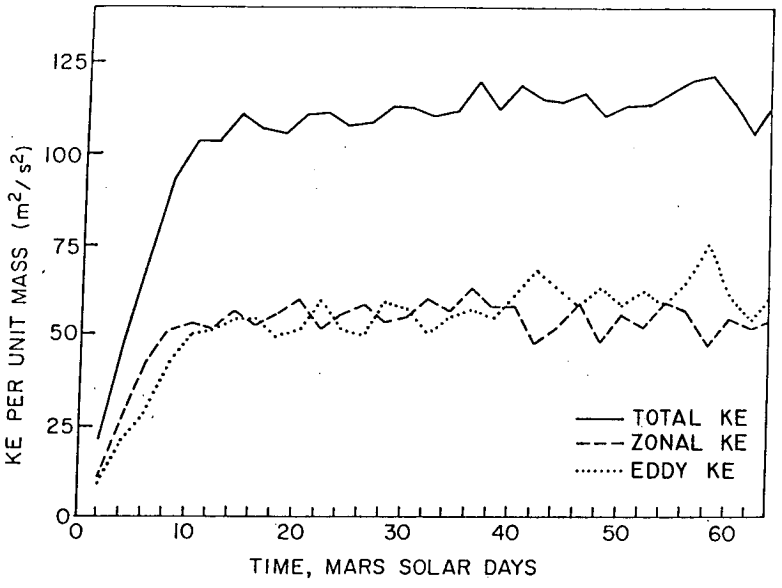

FIG. 5. Evolution of the globally-averaged total kinetic energy and its components: Kinetic energies of the zonally-averaged flow and the eddy flow.

$$T_{CO_2} = 149.2 + 6.48 \ln(0.135 p_s), \quad (4)$$

with p_s in millibars. When T fell to this temperature or below, T_G was set equal to T_{CO_2}, and the release of latent heat of condensation of CO_2 was added to the surface heat balance equation. Thus, the rate of change of CO_2 mass on the surface was given by

$$\partial M_{CO_2}/\partial t = L^{-1}[\sigma T_G^4 + I(\omega/2)^{1/2}(T_G - T_\infty) - (1 - A)F_s - F_{IR} + F_{conv}], \quad (5)$$

where L is the latent heat of condensation of CO_2. $(\partial M_{CO_2}/\partial t)$ was used to infer the value of $\dot{\sigma}$ at $\sigma = 1$. Since $\pi\dot{\sigma}/g$, evaluated at $\sigma = 1$, represents change in mass of the overlying atmospheric column of unit area, the boundary condition used to account for CO_2 phase change was

$$\pi\dot{\sigma} = -g(\partial M_{CO_2}/\partial t) \quad \text{at} \quad \sigma = 1. \quad (6)$$

In the regions where CO_2 condensation occurred, the terms $I(\omega/2)^{1/2}(T_G - T_\infty)$, $(1 - A)F_s$, and F_{conv} in (5) were very small; by far the dominant term was σT_G^4, with F_{IR} playing a secondary role. Hence the values of $\pi\dot{\sigma}$ at $\sigma = 1$, which produced important dynamical effects, were not sensitive to details of the parameterization of albedo, solar absorption, convection or conduction. The mass condensed or sublimed at the surface was assumed to have no velocity relative to the surface, and a temperature equal to T_{CO_2}. The thermodynamic energy equation was modified to allow for gain or loss of internal energy at the surface due to condensation or sublimation at temperature T_{CO_2}. No modification of the momentum equation was required.

In the atmosphere above the surface, temperatures were constrained not to fall below T_{CO_2}, but the mass condensation implied by this constraint was not accounted for. This produced a small error in the results which is discussed further in Section 3.

e. *Input parameters and data*

Basic input parameters are shown in Table A2. The input data also included specification of surface topography (the distribution of Φ at $\sigma = 1$), and surface albedo A_s. Surface topography was obtained from a combination of relevant ground-based and spacecraft data (Kliore *et al.*, 1973; Conrath *et al.*, 1973), and was smoothed for compatibility with the model resolution. Realistic, rapidly varying topography is known to cause significant errors in σ-coordinate models with this version of the Arakawa finite-difference scheme, but these models produce acceptable results with smoothed topography (Halem *et al.*, 1979).[4] The smoothing precludes realistic treatment of such small-scale topographic features as Olympus Mons, however. Fig. 3 shows the topography used; the flat topography used in the South Polar region was due to a lack of good measurements at the time of the simulation.

Fig. 4 shows the distribution of A_s. Relative albedo variations were provided by James Cutts from his analysis of Mariner 9 images, and these were normalized to a bolometric albedo of 0.24 (Irvine *et al.*, 1968). When CO_2 ice occurred on the surface A_s was set equal to 0.6. A small subliming CO_2 polar cap, intended to simulate the observed seasonal residual cap (Briggs, 1974), was maintained at lati-

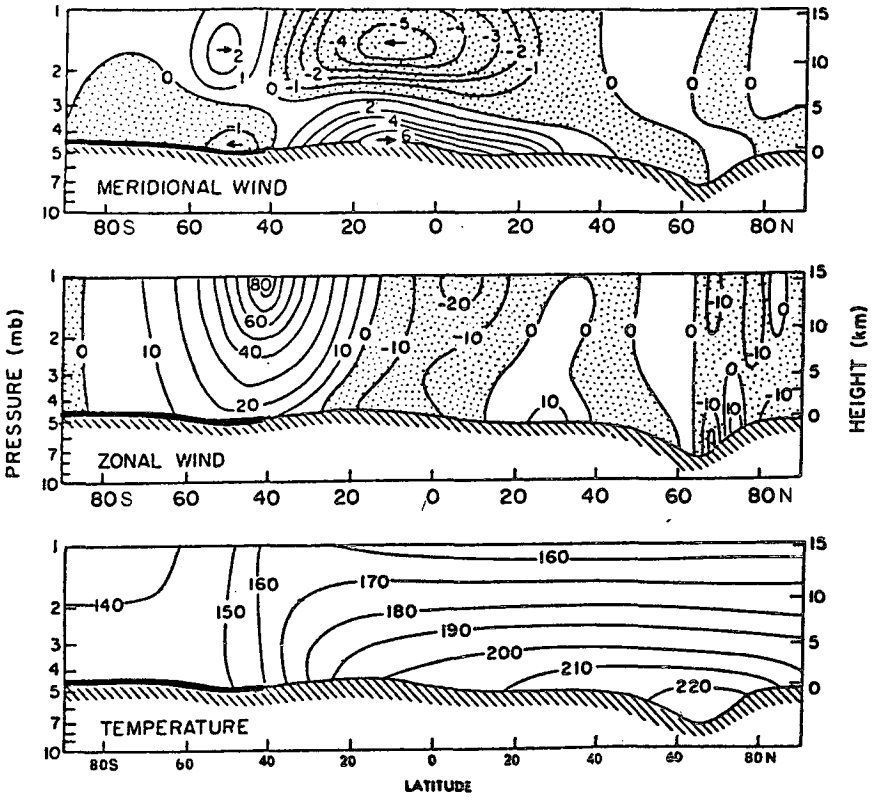

FIG. 6. Model generated zonal and time averaged distributions of temperature (lower), zonal wind (middle, positive eastward), and meridional wind (upper, positive northward). Units are K and m s^{-1}. Heavy line at the surface indicates extent of CO_2 ice cap.

tudes 85 and 90°N until $L_s = 100$.[4] The albedo effect of a permanent ice cap was maintained at 90°N thereafter.

The integration was initiated from a resting isothermal state (200 K) with declination and distance of the sun initialized to areocentric longitude $L_s = 82°$. The integration was for 65 sols, with solar declination and distance varying continuously with the change in Martian season, up to values corresponding to $L_s = 112°$.

3. Results

a. Spinup

Because of the rapid thermal adjustment characteristic of the Martian heating processes, an approximate statistically steady state in the temperature and wind fields was achieved within less than 20 sols. This is illustrated by the growth of kinetic energy (Fig. 5). The total kinetic energy and its two components, the kinetic energy of the zonally-averaged flow (zonal kinetic energy) and the kinetic energy of departures of flow from the zonal average (eddy kinetic energy), reach nearly constant levels by about sol 12. These two components are nearly equal in magnitude, and their fluctuations are negatively correlated. Similar behavior was observed in the northern winter solstice experiment of Paper I, although the kinetic energy levels are substantially lower in the present experiment. The lower kinetic energy level is primarily due to the weaker tropical winds, and is partly a consequence of the seasonal difference: the solar heating of Mars is ~40% smaller at southern winter solstice than at northern winter solstice. The inclusion of topography may also contribute to the kinetic energy reduction.

Except as indicated, the results presented below correspond to averages over the last 10 sols of the run. This period only includes about two oscillations of the zonal kinetic energy, so that in retrospect, a longer averaging period would have been desirable.

b. Zonally-averaged temperature and wind

Fig. 6 shows zonally-averaged temperature and wind generated by the model, with the contours drawn by subjective interpolation between the data

[4] Areocentric longitude of the sun L_s in Mars centered coordinates relative to the fixed star background. L_s is the seasonal index with $L_s = 0°$ corresponding to northern spring equinox.

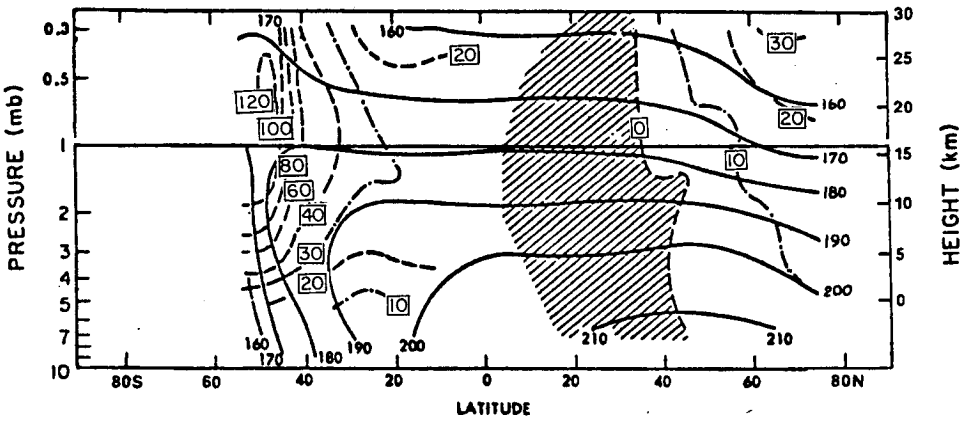

FIG. 7. Cross section of zonally-averaged temperature (K) and geostrophic zonal wind (m s^{-1}) based on Mariner 9 IRIS data between L_s = 43 and L_s = 54 (approximately early May in analogous terrestrial season).

points at the three levels. As in Paper I, there is a broad region of relatively warm and uniform temperatures in the tropics and the summer hemisphere, a region of large horizontal temperature gradient and high static stability between 30 and 50° in the winter hemisphere, and a nearly isothermal region poleward of 50°S. A surface CO_2 ice cap has formed in the winter polar region with its boundary between 40 and 45°. The simulated zonal winds are eastward in the winter middle and high latitudes with an intense jet at the upper level near the edge of the polar cap, westward in the tropics of both hemispheres, and eastward in the summer subtropics. As in Paper I, the summer subtropical low-level eastward flow is found at the poleward limit of the cross-equatorial meridional circulation. At high northern latitudes, the mean zonal winds have a small scale structure connected with the small-scale zonally-symmetric variation in the topography and the meridional gradient of heating produced by the high albedo of the small residual polar cap. Because these small-scale zonal wind features are not well resolved by the model grid, their magnitude may be partly a spurious computational effect.

Some comparisons can be made with observed Martian temperature distributions. Fig. 7 is a temperature cross section obtained by averaging Mariner 9 IRIS soundings over the seasonal period L_s = 43–54.[5] This is the closest seasonal period for which we were able to obtain enough data to construct a reasonably complete meridional temperature cross section. The winds shown in Fig. 7 are the geostrophic winds obtained by assuming negligible surface wind. Although the comparisons differ with respect to season and the neglect of the surface wind, Figs. 6 and 7 show striking similarities: (i) weak horizontal temperature gradients except in the winter subpolar region; (ii) a very strong horizontal temperature gradient within that region and correspondingly strong eastward winds aloft; and (iii) large static stability and a high-level temperature maximum in the winter subpolar region. There are also some understandable differences: (i) outside of the winter subpolar zone, the simulated static stability is smaller than the observed, undoubtedly as a consequence of our having neglected the dust aerosol heating (Pollack *et al.*, 1979); (ii) the region of strong poleward temperature gradient and zonal wind is farther from the south pole in the calculation than in these observations as a consequence of the seasonal difference: The polar cap boundary is closer to the pole at the time of these observations than at the time corresponding to the simulation.

The simulated mean meridional circulation (Fig. 6, upper panel) shows a very strong cross-equatorial flow, northward at the lower levels and southward aloft. It is much more intense than the Earth's tropical meridional circulation; but it is weaker than the corresponding circulation of *I*, probably partly because of the greater distance from the sun. South of 40°S, there is a thermally-indirect cell. Unlike its counterpart in the Earth's atmosphere, the Ferrell cell, in which the mass transports of the upper and lower branches are nearly in balance, here the lower branch is carrying substantially more mass toward the pole than the upper branch removes. This is the uniquely Martian process of a net mass flow toward the condensing winter polar cap (see Paper I and the next subsection).

Fig. 8 shows simulated zonally- and time-averaged vertical velocities (dp/dt) at the two internal inter-

[5] Results of the IRIS experiment have been described in papers by Hanel *et al.* (1972), Conrath *et al.* (1973) and Conrath (1975). The data on which Fig. 10 is based were kindly provided by Dr. B. Conrath of the Goddard Space Flight Center.

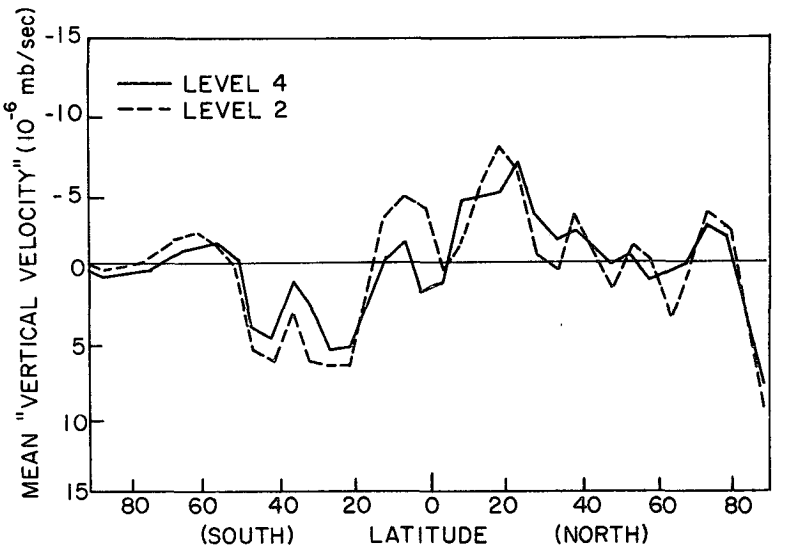

FIG. 8. Time and zonally averaged σ-coordinate vertical velocities (dp/dt), illustrating the vertical branch of the overturning circulation. (The negative values, corresponding to ascending motion, are above the abscissa; descending motion is below.)

faces (levels 2 and 4 of Fig. 1). Negative values are plotted above the abscissa indicating upward motion. The vertical velocity produced by the model is generally somewhat noisy, and the noise appears even in the time and zonal averages. Nevertheless, the strong cross-equatorial thermally-direct circulation and the weaker indirect circulation in the winter hemisphere midlatitudes show clearly in these meridional profiles.

c. *Mass, heat and momentum balances*

To gain insight into the roles of various dynamical processes in the Martian atmosphere, we describe the transports and sources and sinks of mass, heat, and momentum in this section. We let $[(\ )]$ denote a longitudinal average along constant σ, $\overline{(\ )}$ denote an average over time period t_a, and $(\ )^*$ and $(\ )'$ be the departures from these respective averages. Then the zonally-averaged continuity equation for any intrinsic variable Q can be expressed in the form

$$t_a^{-1}\{[\pi Q]_{t=t_a} - [\pi Q]_{t=0}\} \approx -\frac{1}{a\cos\phi}\frac{\partial}{\partial\phi}\{\cos\phi([\overline{\pi v}][\bar{Q}] + [(\overline{\pi v})^*\bar{Q}^*] + [\overline{(\pi v)'Q'}])\}$$

$$-\frac{\partial}{\partial\sigma}\{[\overline{\pi\dot{\sigma}}][\bar{Q}] + [(\pi\bar{\dot{\sigma}})^*\bar{Q}^*] + [\overline{(\pi\dot{\sigma})'Q'}]\} + [\bar{S}_Q], \quad (7)$$

where S_Q is the source term for Q. The first two terms on the right represent, respectively, convergences of the meridional and vertical transports of Q, where each transport has three components: transport by the mean meridional circulation, transport by the stationary eddies, and transport by transient eddies.

If we set $Q = 1$, the continuity equation representing the mass balance is obtained; in this case, all the eddy transports and $[\bar{S}_Q]$ vanish. CO_2 condensation and sublimation are accounted for by the boundary term, $\pi\dot{\sigma}$ at $\sigma = 1$ [Eq. (6)].

Setting $Q = c_pT + \Phi + \frac{1}{2}\mathbf{v}^2 \approx c_pT + \Phi \equiv h$, we obtain the conservation equation for enthalpy h, the so-called "heat balance equation." The kinetic energy term $\frac{1}{2}\mathbf{v}^2$ is negligible if the Mach number of the flow is small. S_h includes radiative and convective heating.

Finally, if we set $Q = a\cos\phi(u + \Omega a\cos\phi) \equiv M$, the zonal angular momentum per unit mass for zonal wind u, the angular momentum balance equation is obtained. S_M includes the surface wind stress and the large-scale pressure torques exerted by the mountains, as well as the frictional stresses between layers due to the Richardson number adjustment of velocity.

An alternative useful form for Eq. (7) is

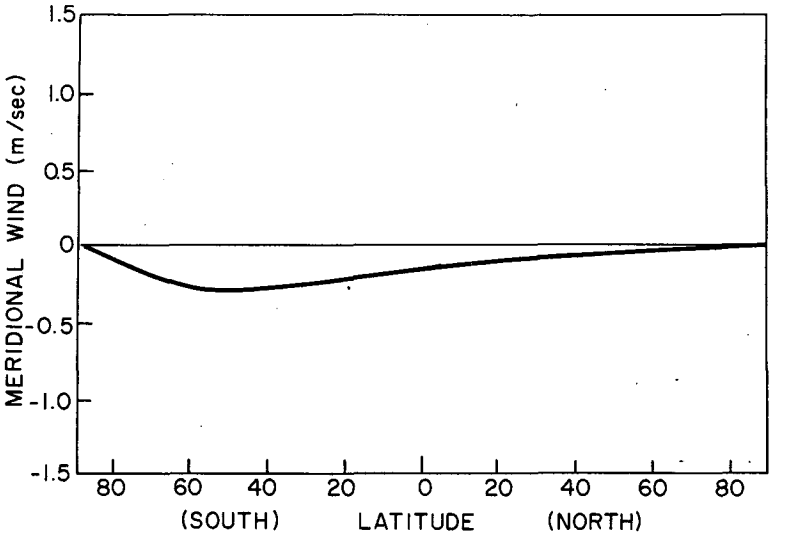

FIG. 9. Latitudinal distribution of the condensation flow.

$$t_a^{-1}\{[\pi Q]_{t=t_a} - [\pi Q]_{t=0} - [\bar{Q}]([\pi]_{t=t_a} - [\pi]_{t=0})\}$$

$$\approx -a^{-1}[\pi\bar{v}]\frac{\partial}{\partial\phi}[\bar{Q}] - [\pi\dot{\bar{\sigma}}]\frac{\partial}{\partial\sigma}[\bar{Q}]$$

$$-\frac{1}{a\cos\phi}\frac{\partial}{\partial\phi}\{\cos\phi([(\pi\bar{v})^*\bar{Q}^*] + [\overline{(\pi v)'Q'}])\}$$

$$-\frac{\partial}{\partial\sigma}\{[(\pi\dot{\bar{\sigma}})^*\bar{Q}^*] + [\overline{(\pi\dot{\sigma})'Q'}]\} + [\bar{S}_Q] \approx 0. \quad (8)$$

We use this form to interpret the results for two reasons. First, the intrinsic variables Q are roughly constant over the 10 sol sampling period so that the terms on the left side nearly cancel each other. This is despite decreasing values of π over the interval as a result of mass condensation in the winter polar cap. Consequently, there is approximate balance between the terms on the right. Second, it is very difficult to evaluate the contribution to change in Q over individual layers from the convergence of the mean meridional circulation transport because it contains two terms which are large, nearly compensating, and imperfectly sampled. This difficulty does not occur when the mean meridional circulation contribution is evaluated in the advective form as in Eq. (8).

1) MASS BALANCE

The vertically integrated mean northward mass flow velocity or "condensation flow", $[\bar{\pi}]^{-1}\int_0^1[\pi\bar{v}]d\sigma$,

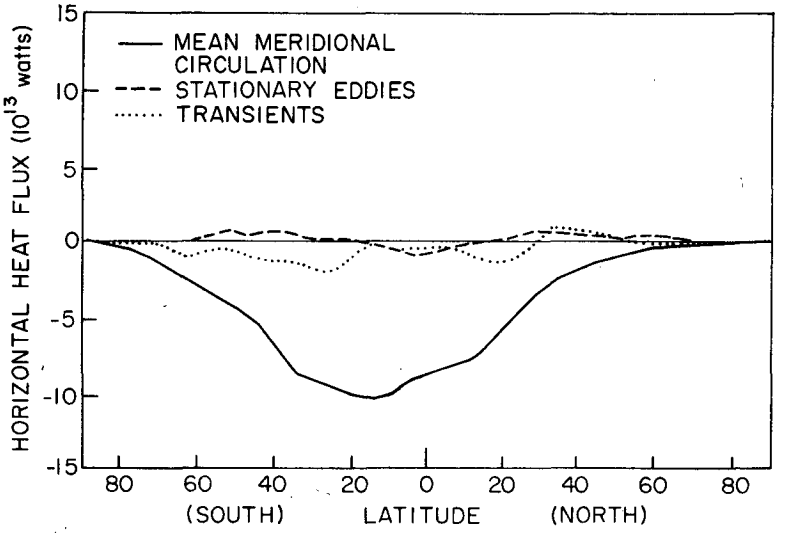

FIG. 10. Flux of enthalpy ($h = c_pT + \Phi$) due to mean meridional circulation, stationary eddies and transient eddies.

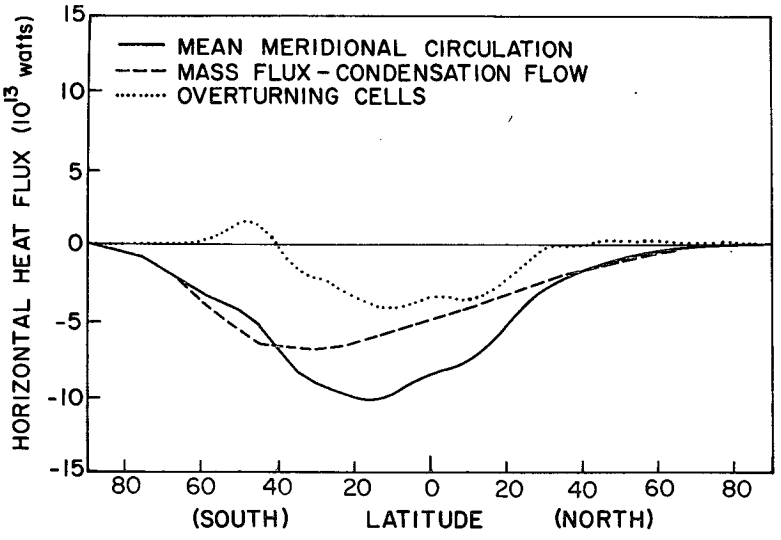

FIG. 11. The flux of h by mean meridional circulation and its components: the condensation flow and the overturning circulation cells.

is shown in Fig. 9. There is a substantial mass flow velocity toward the winter polar cap reaching 0.27 m s^{-1} near 55°S. This is a consequence of CO_2 condensation at the cap surface, and is similar to the condensation mass flux obtained in Paper I. It corresponds to a rate of pressure drop of 0.011 mb sol^{-1} averaged over the planet, or to a total mass loss rate of 4.2×10^{13} kg sol^{-1}. This rate of pressure drop agrees with the rate observed by the Viking landers at the same season (Hess *et al.*, 1977). It also is in rough agreement with the mass loss calculated by Leighton and Murray in 1966 on the basis of a simple radiation balance model. This is discussed further in the next subsection.

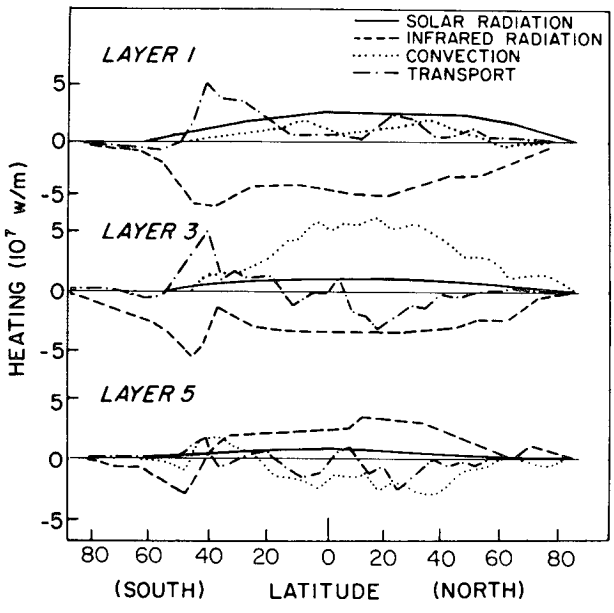

FIG. 12. Contributions to the heating and cooling of each layer. The component labeled "transport" includes advection of h by the mean meridional circulation, and convergence or divergence of the vertical components of h flux by stationary and transient eddies [see Eq. (8)].

2) HEAT BALANCE

Fig. 10 shows the vertically-integrated northward transport of h due to each transport component: mean meridional circulation, stationary eddies and transient eddies. The flux due to the mean meridional circulation is southward in all latitudes and much larger than either of the eddy fluxes. The transient eddy flux is generally in the direction of decreasing h (or T); the stationary eddy flux is generally weaker than the transient eddy flux, and is countergradient in both northern and southern midlatitudes.

The flux of h due to the mean meridional circulation can be separated into the part due to the condensation flow and a residual which we term the "overturning circulation" (Fig. 11). The condensation flow dominates, although the contribution of the overturning circulation is also large. Even the thermally indirect cell south of 40°S produces a transport as large as that of the transient eddies and tends to cancel the poleward transport of the latter.

In Fig. 12, the latitudinal distributions of the several contributions to the heat balance of each layer are displayed. The transport term shown includes the heating by horizontal and vertical advection by the mean meridional circulation and by convergence of the vertical eddy flux by both stationary and transient eddies. The convergence of the horizontal eddy flux was not calculated for the individual layers, but it is generally smaller than the

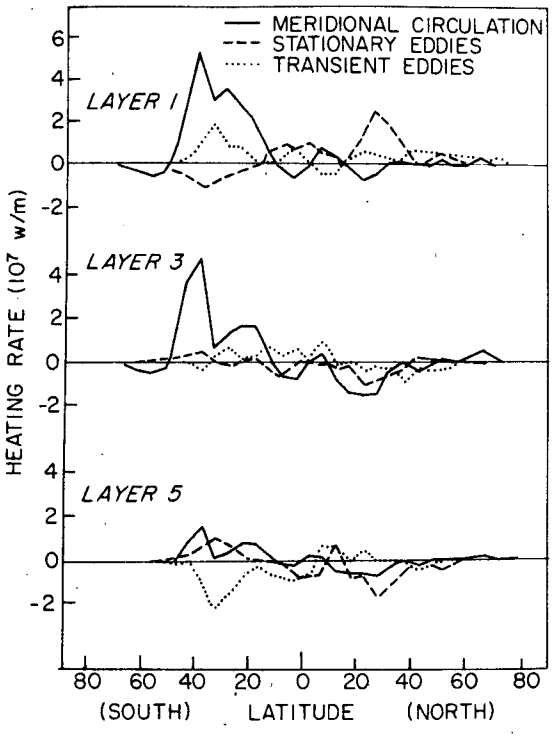

FIG. 13. The "transport" contribution to heating or cooling of each layer shown in Fig. 15 is further broken down into advection of h by the mean meridional circulation and convergence or divergence of the vertical components of h flux by stationary and transient eddies.

contributions shown. The figure does not show exact balances, partly because of neglect of the horizontal eddy flux convergence, but also because of residual transience over the 10 sol averaging period as well as sampling error (160 sample times contribute to each average). Despite the sources of inaccuracy the relative magnitudes are clear.

In the lowest layer, the balance is primarily between gain of heat by infrared radiative exchange with the underlying warmer ground, and removal of heat by convection. Just equatorward of the polar cap edge, convection heats this shallow layer. Solar radiation makes only a small contribution, and transport plays a variable role, generally cooling the layer in the tropics and summer hemisphere and warming it between 40 and 50°S.

In the middle layer, the balance tends to be between convective heating and infrared cooling. The transport generally tends to cool the summer hemisphere. It strongly warms the winter hemisphere near the edge of the condensing polar cap, where the infrared heat loss is large. Part of the convective heating of the middle layer corresponds to the cooling of the lower layer by convective adjustment, and the additional part is a heat transfer from the surface.

In the upper layer, the convective heating is weak, but it still contributes, along with solar radiation and transport heating, to balancing the large infrared radiative loss to space. Between 10 and 40°S, the balance is mainly between the large infrared radiative loss and warming by transport.

Fig. 13 shows separately the contributions to the transport heating by meridional circulation and eddies. The mean meridional circulation cools the atmosphere where the vertical motion is upward, and warms it where the vertical motion is downward, but the winter hemisphere warming greatly exceeds the summer hemisphere cooling because of the difference in the winter and summer static stabilities. The vertical heat flux by transient eddies

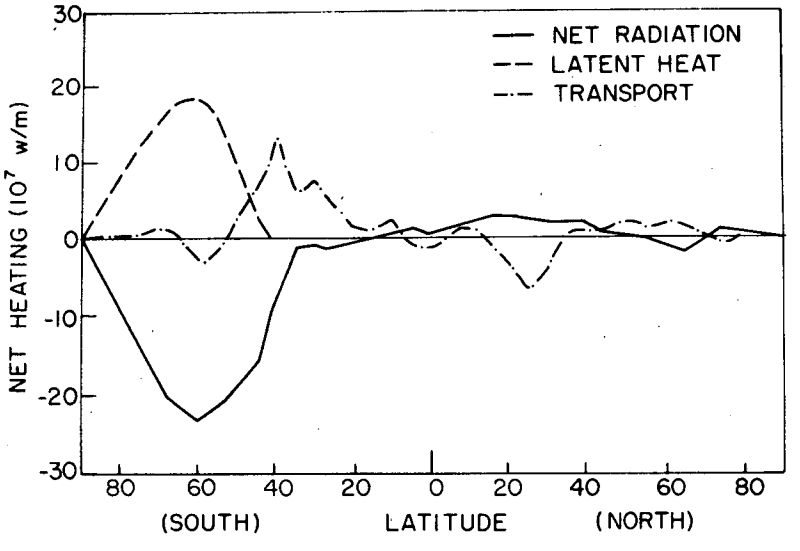

FIG. 14. Contributions to the vertically-integrated zonally averaged heat balance.

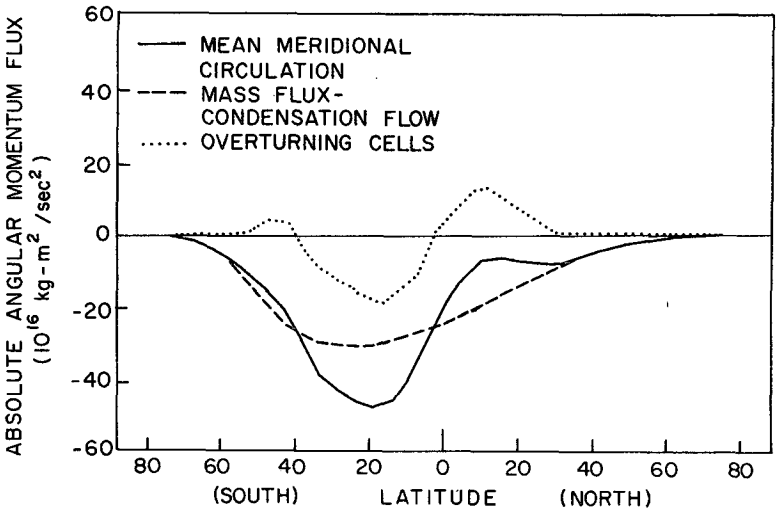

FIG. 15. Flux of absolute angular momentum ($M = a^2\Omega \cos^2\phi + au \cos\phi$) by the mean meridional circulation and its components: the condensation flow and the overturning circulation cells.

is upward in the 20–50°S region, thereby warming the upper layer and cooling the lowest layer. In the same latitude zone, downward heat transfer by the stationary eddies produces exactly the opposite effect, cooling the upper layer and warming the lower layer. On the other hand, between 20 and 40°N, the stationary eddies produce a substantial upward heat transfer. In the same region, there is weaker upward heat flux by transient eddies between the upper and middle layers. These properties of the eddy heat fluxes will be used to deduce a qualitative dynamical picture of the eddies.

In Fig. 14, the terms contributing to the vertically-integrated heat balance at each latitude are displayed. Because this is the planetary heat balance, the heat balance of the ground plus atmosphere, convective heating is zero. The net radiation is weakly positive in the tropics and summer subtropics, but strongly negative over the winter polar cap where latent heat release tends to balance it. This balance is not exact, in part because atmospheric temperatures are constrained from falling below the CO_2 frost point. As mentioned in Section 2, this corresponds to an implicit heat source south of 50°S, not shown in Figs. 12–14, and to a small implicit condensed mass storage, not accounted for in the mass balance (precipitation of CO_2 from the atmosphere was not allowed for). Fig. 12 shows that most of this heating occurs in the middle layer. The neglected implicit mass storage

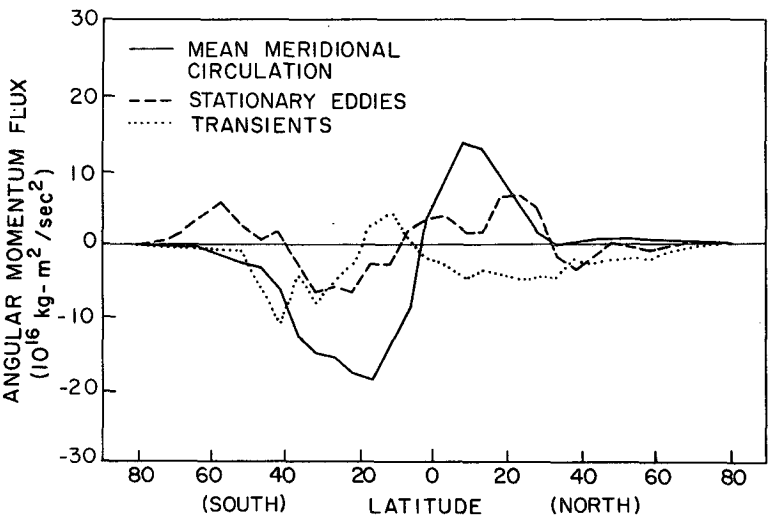

FIG. 16. Flux of relative angular momentum ($M_r = au \cos\phi$) by the mean meridional circulation and the stationary and transient eddies.

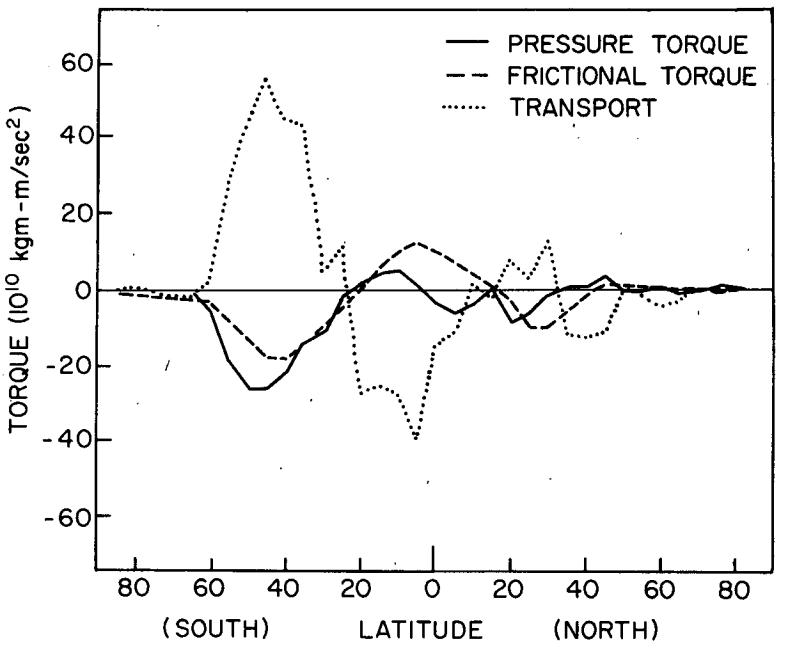

FIG. 17. Contributions to the angular momentum balance: convergence of the angular momentum transport, surface friction torque and mountain pressure torque.

amounts to ~20% of the storage at the ground, and thus implies ~20% underestimates of the total CO_2 mass loss rate, rate of pressure fall, and mass flow circulation intensity. This error may have been fortuitously compensated to a large degree by our assumption of unit emissivity for the CO_2 ice-covered surface. Ditteon and Kieffer (1979) have shown that the thermal emissivity of CO_2 ice may be quite low, and neglect of this effect could have led to an overestimate of the CO_2 condensation rate by as much as 20%. The transport contribution to heat balance calculated from Eq. (8) includes both the convergence of the vertically-integrated meridional eddy fluxes of h, and heating by the mean meridional circulation. The heating by the mean meridional circulation is the main contributor to this term in most latitudes, and noise in this quantity is a consequence of the noise in the calculated vertical velocities.

In the simulation, the heat and momentum transports *per unit atmospheric mass* are very large, and so they control the evolution of the temperature and wind fields. But the total mass of the atmosphere is very small, and so the total, vertically-integrated, meridional heat transport is small. (The total mass in unit column of atmosphere on Mars is almost two orders of magnitude smaller than it is on Earth.) Therefore, the assumption made by Leighton and Murray (1966) was correct, namely, that the formation of the CO_2 polar cap would be controlled almost entirely by the radiation field; and Figs. 10, 11, and 14 show this.

3) ANGULAR MOMENTUM BALANCE

The transport of absolute angular momentum M, like that of h, is accomplished mainly by the mean meridional circulation. Fig. 15 shows the total flux of M by the mean meridional circulation and its components: flux by the condensation flow and flux by the overturning circulation. The former dominates at all latitudes; the latter arises mainly from correlations between the overturning meridional flow and the mean zonal wind $[\bar{u}]$. Thus the overturning cells transport M toward the pole in each hemisphere, except in the region 40–55°S where the thermally-indirect overturning circulation interacts with the eastward vertical wind shear.

The eddies also transport angular momentum. The transports by the stationary and transient eddies are shown in Fig. 16. This figure also shows the transport of relative angular momentum by the mean meridional circulation (condensation flow plus overturning cells); the transport of planetary angular momentum, $a^2\Omega \cos^2\phi$, has been subtracted out. These transports are much smaller than the transport of planetary angular momentum by the condensation flow, which is almost non-existent in the Earth's atmosphere. There are two regions of convergence of the poleward stationary eddy flux of eastward angular momentum: 35–55°S and 20–35°N. Both are regions of maximum eastward wind. Elsewhere there is generally weak flux divergence. This convergence-divergence pattern is consistent with that expected for dissipative stationary waves

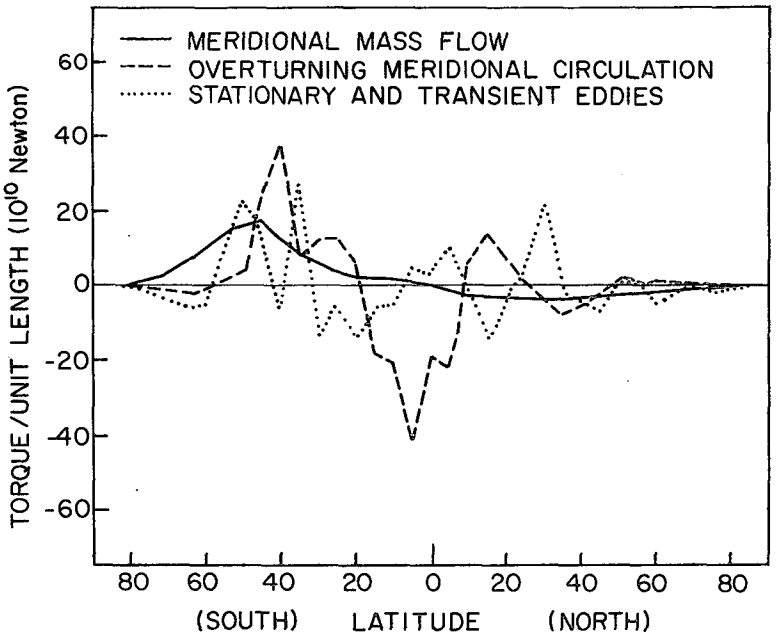

FIG. 18. Angular momentum transport convergence (torque) due to the mass flux—condensation flow, the overturning cells and the stationary and transient eddies.

forced by flow over topography. Stationary waves are generated most effectively in regions of eastward zonal winds, since the Rossby wave response can be excited there. As first described by Eliassen and Palm (1960), the energy of the stationary waves flows away from such regions as does westward (negative) angular momentum. This is equivalent to a convergence of eastward (positive) angular momentum into the eastward wind maxima. Held (1975) discusses this process for quasi-geostrophic waves.

The transient eddies, on the other hand, produce maximum convergence of eastward angular momentum between 40 and 50°S, just poleward of the main eastward jet; they produce divergence of eastward angular momentum from the equatorward side of the jet to ~10°S. Near the equator there is angular momentum flux convergence by transient eddies which largely compensates the divergence produced by the stationary eddies in that region. This pattern of angular momentum transport by transient eddies, with the poleward transport maximum at the latitude of the jet, convergence poleward of the jet and divergence equatorward, is similar to that found by Blackmon *et al.* (1977), and by many earlier investigators, for the mean jet stream region in the Earth's atmosphere. On the Earth, this distribution is produced by the transient wave cyclones that form in the baroclinically unstable flow on the poleward side of the jet.

Fig. 17 shows the terms contributing to the angular momentum balance of the atmosphere within each latitude belt. Again, residual transience and noise in the sampled output preclude precise balance. The transport term includes the contribution by the mean meridional circulation and the stationary and transient eddies. The mountain pressure torque was evaluated from the distribution of the surface pressure variable π, using the relation

$$\text{Mountain torque} = a\cos\phi \int_0^{2\pi} \pi \frac{\partial \Phi_s}{\partial \phi} d\lambda, \quad (9)$$

where ϕ is latitude, λ longitude, and Φ_s surface geopotential. This term is easily evaluated from the model output, although it is susceptible to sampling error. The pressure torque on the atmosphere is negative where high pressure is correlated with eastward rising slopes. The figure shows that surface friction and pressure torque make large and comparable contributions to balancing the angular momentum transport convergence.

Fig. 18 shows the contributions of the different transport terms to the angular momentum balance. All of them contribute significantly to the maintenance of the winter middle-latitude eastward surface winds, but poleward of 60°S, the eastward winds are maintained only by the condensation flow. The summer hemisphere eastward surface winds are maintained by the overturning circulation and eddies, which oppose the effect of the condensation flow. The eddies, and the stationary eddies in particular, play a somewhat larger role in maintaining the winter hemisphere eastward winds than they did in Paper I.

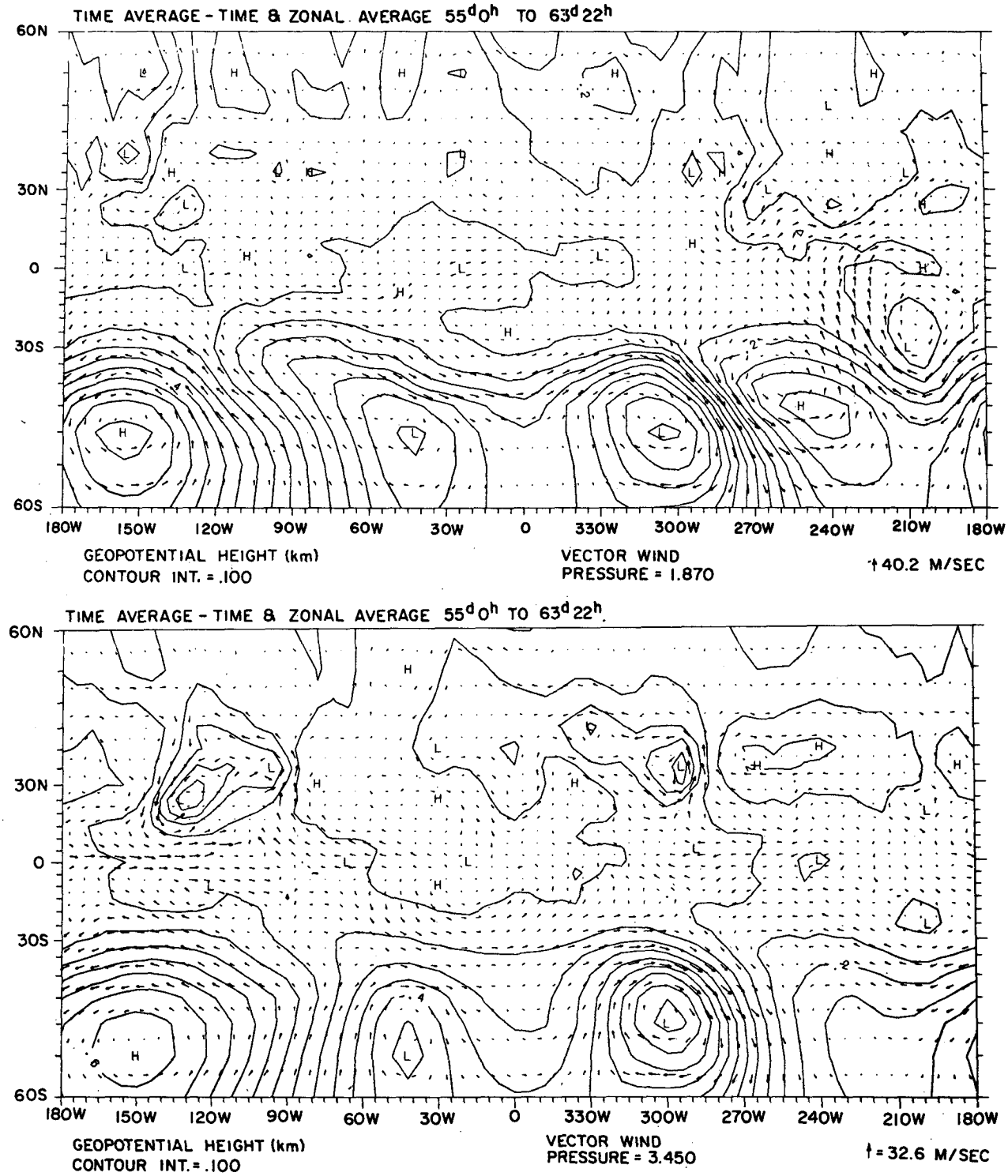

FIG. 19. Structure of the stationary eddies illustrated with time-averaged vector wind and geopotential perturbations at the 1.87 mb level (upper) and at the 3.45 mb level (lower). The zonally averaged winds and geopotentials have been subtracted. Winds are scaled to maxima of 40.3 m s^{-1} (upper) and 32.6 m s^{-1} (lower). Contours are 0.1 geopotential km.

d. The stationary eddies

Fig. 19 displays the time-averaged wind and geopotential perturbations, shown as departures from the zonal means at the 1.87 and 3.45 mb pressure levels. The most striking feature is the large-amplitude ridge-trough system in the eastward wind belt of the winter hemisphere. There is a particularly

prominent ridge near 150°W and trough in Hellas (300°W), with secondary troughs near 50 and 200°W and ridges near 350 and 240°W. These features are only slightly out of phase between the two levels and have comparable amplitudes at both levels. We interpret them as quasi-barotropic waves kinematically forced by the topography. According to Fig. 3, the major ridge in the Tharsis region extends southward along longitude 100°W to ~50°S, and the conservation of potential vorticity in the upslope and downslope flows on the western and eastern sides of this topographic ridge produces the ridge in the velocity field near 150°W and the downstream trough near 45°W. Similarly, the trough and ridge in the flow field, at 300°W and 240°W, are produced by the downslope and upslope flow on the western and eastern sides of the Hellas depression at 290°W. The same process is largely responsible for producing the stationary waves in the lee of the mountain barriers of western North America and east Asia during winter. Note the marked SE-NW tilt of the waves at the upper level between 30 and 50°S, indicative of the poleward momentum flux already discussed.

Fig. 19 also shows another kind of stationary wave system, in the summer hemisphere, located between 15 and 35°N. Its major features are the low-level low-pressure centers over the uplands near 130 and 290°W. The phase of these systems reverses with height so that the convergent cyclonic flow at low levels is replaced by divergent anticyclonic flow aloft. We interpret these as disturbances forced by the thermal influence of topography, similar to the surface lows which develop in summer over the Asian and North American uplands. This system is most prominent in the zone of eastward flow where Rossby wave response is possible.

The stationary wave disturbances in the Southern Hemisphere are qualitatively similar to those obtained by Mass and Sagan (1976) who used a two-level quasi-geostrophic model, and the waves in both hemispheres closely resemble those found by Webster (1977) who used a two-level linearized primitive equation model. We conclude that the nonlinear processes are not crucial for these stationary waves, and their main properties can be understood in terms of linear wave theory. Although the severe vertical truncation inherent in all of these models may distort the results, we do not believe that this is a serious problem. Webster has pointed out that the strong radiative damping which characterizes Mars will smooth out the finer detail in the vertical structure of these waves.

e. Kinetic energy budget

We have not made a quantitative evaluation of the kinetic energy budget of the model results, principally because of the difficulty of defining available potential energy in a circulation which is influenced by such large amplitude topography and which has a condensation flow. Nevertheless, we can qualitatively sketch some elements of the conversion between zonal available potential energy (ZAPE), eddy available potential energy (EAPE), zonal kinetic energy (ZKE), and eddy kinetic energy (EKE) for two regions: The region of the topographically-forced stationary waves (20–60°S), and the region of the thermally-forced stationary waves (15–35°N) [see Lorenz (1955) for definitions of these quantities and the conversions between them for an atmosphere with a horizontal lower boundary]. This is indicated schematically in Fig. 20, where the dashed-line arrows indicate the conversions associated with the stationary eddies and the dotted-line arrows the conversions associated with the transient eddies.

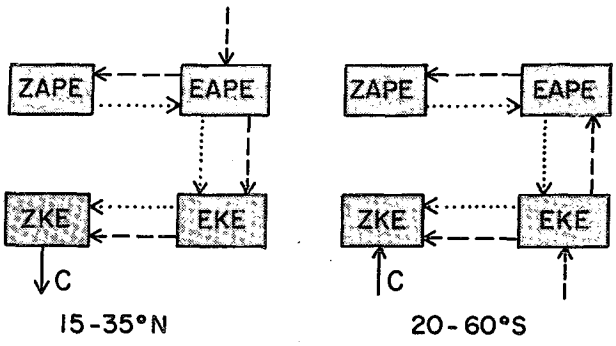

FIG. 20. Qualitative illustration of the kinetic energy balance in two latitude belts: summer tropics (left) and winter midlatitudes (right). Dashed arrows: stationary wave contributions; dotted arrows: transient wave contributions; solid arrows: generation of ZKE by condensation flow (*C*).

Fig. 10 showed that in the region 20–60°S the stationary eddies transport heat against the mean meridional temperature gradient, so that they convert EAPE to ZAPE. They also transport heat downward, thereby converting EKE to EAPE. The transport of momentum is toward the zonal jet, so that the stationary eddies convert EKE to ZKE. This cycle, in which EKE is converted to both EAPE and ZKE, is characteristic of kinematically-forced waves. The only adequate source for the EKE of these waves is the work done by the positive correlation of pressure and vertical velocity on the slopes of the mountains. This is indicated by the dashed arrow entering the EKE box from below. The ZKE generated in this way is removed by mountain pressure torque as well as by surface friction.

In the region 15–35°N, the stationary eddy contributions to the energy cycle are quite different. Fig. 13 showed that the stationary eddy heat transport is upward, so that there is conversion from EAPE to EKE. Momentum transport is toward the eastward wind maximum so that EKE is again

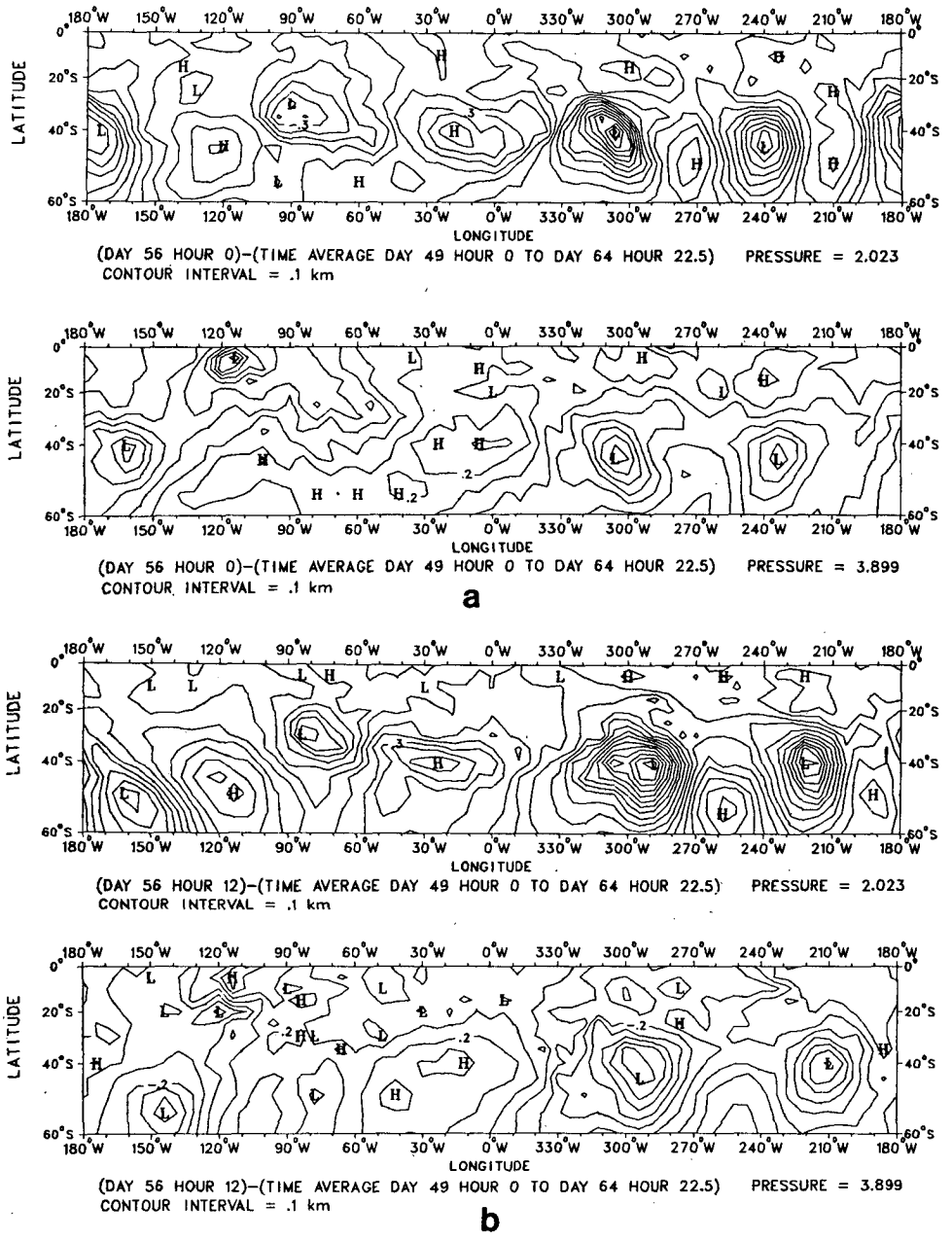

FIG. 21. Example of a synoptic sequence. Upper three panels: geopotentials at the 2.023 mb pressure level on sols 56.0, 56.5 and 57.0 shown as departures from the 16 sol mean. Lower three panels: the same at the 3.899 mb level. Note that the low center near 115°W, 5°S at 3.899 mb is part of the diurnal thermal tidal oscillation over the Tharsis Ridge, and is not closely related to the eastward moving midlatitude waves.

being converted to ZKE (Figs. 16 and 19), and the small horizontal heat transport, is again countergradient (Fig. 10), so that EAPE is being converted to ZAPE, though at a much slower rate than in the south. These processes are characteristic of thermally-driven disturbances. In order to compensate the losses of EAPE in the stationary waves, there must be production of EAPE through radiative and convective processes. This is indicated by the dashed arrow entering the EAPE box, for 15–35°N, from above.

The process influencing the ZKE within these restricted domains cannot be adequately isolated because transports across the lateral boundaries are important. However, one influence which does not appear in the terrestrial kinetic energy budget is

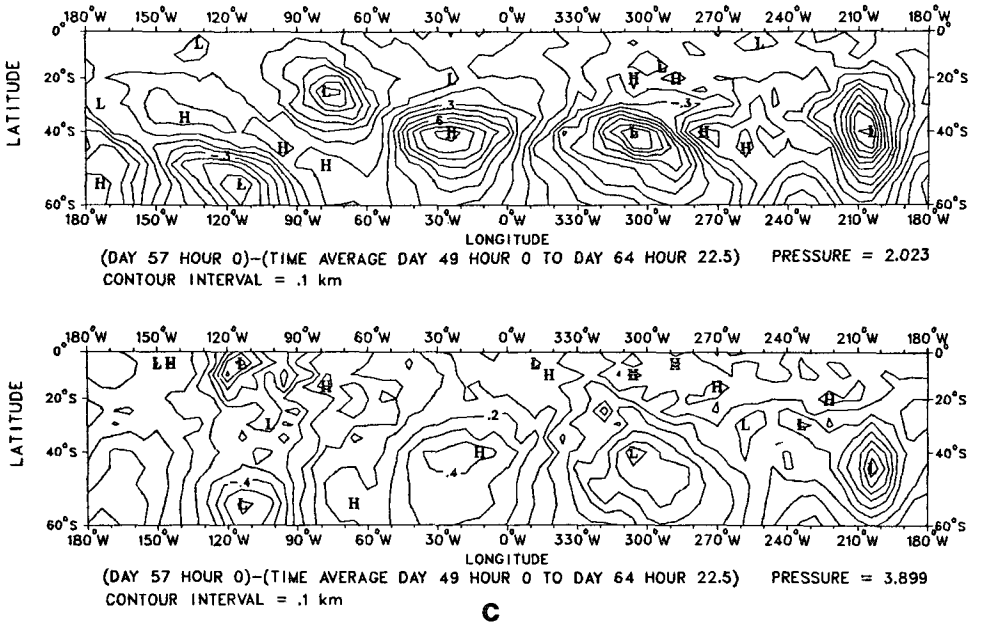

FIG. 21. (*Continued*)

significant here: The condensation mass flow can generate or destroy ZKE as a consequence of its Coriolis torque. Thus, in the region 20–60°S, ZKE is being strongly generated within the eastward current by the poleward condensation flow, while between 15 and 35°N, ZKE is being destroyed within the eastward current by the equatorward condensation flow (solid arrows marked C in Fig. 20).

Overall, ZKE is being generated by the thermally-direct overturning circulation north of 40°S, and being destroyed by the thermally-indirect overturning circulation south of 40°S. This leads us to inquire as to what maintains the indirect overturning cell in the southern hemisphere. One can explain the large magnitude of this circulation component as follows: The condensation flow, the stationary eddies, and the transient eddies (to be discussed below) all generate ZKE, but the ZKE in this region must correspond to zonal winds which are in thermal wind balance with the radiatively-imposed temperature distribution and must also provide sufficient angular momentum loss at the surface to balance the angular momentum sources elsewhere at the planet's surface. If the frictional removal of ZKE is inadequate to satisfy all of these constraints, a strong thermally-indirect circulation, which converts ZKE to ZAPE, will develop to fill the breach. On the basis of this argument, we can see that the magnitude of the indirect circulation is sensitive to our formulation of friction. A source of friction which has been omitted in our model is the interaction of topographically-produced gravity waves with the zonal wind. Observations show that such gravity waves are ubiquitous in Martian middle latitudes during winter (e.g., Briggs and Leovy, 1974). If they provide a significant frictional drag on the zonal wind, they would reduce the magnitude of the thermally-indirect circulation. A secondary consequence would be a weakening of the meridional temperature gradient in this region since the indirect circulation transfers heat away from the pole. This could, in turn, lead to a slight reduction in the CO_2 condensation rate in the outer part of the polar cap zone.

f. Structure and motion of the transient waves

Several effects of the transient waves have already been discussed. The structure and motion of these waves at two constant pressure levels, are illustrated in Fig. 21, which displays departures of the geopotential from a 16 sol time average. Looking, first, at the upper level wind and geopotential fields, (upper panels), we see three moving low-pressure systems south of 20°S. Near 45°S, on sol 56.0, these are located at about 240, 95 and 175°W. They can be seen to move eastward during the sol that follows and in some cases to intensify with time. Comparing the upper and lower panels, we see that these three waves move coherently and that they generally tilt westward with height. This structure is consistent with the previously described poleward and upward transient eddy heat fluxes in the 20–60°S region (Figs. 10 and 13), and we infer that these are the eddies responsible for those heat fluxes, as well as for the transient eddy momentum fluxes (Fig. 16). The phase speed of these waves is ~15–20 m s^{-1}, comparable to the mean

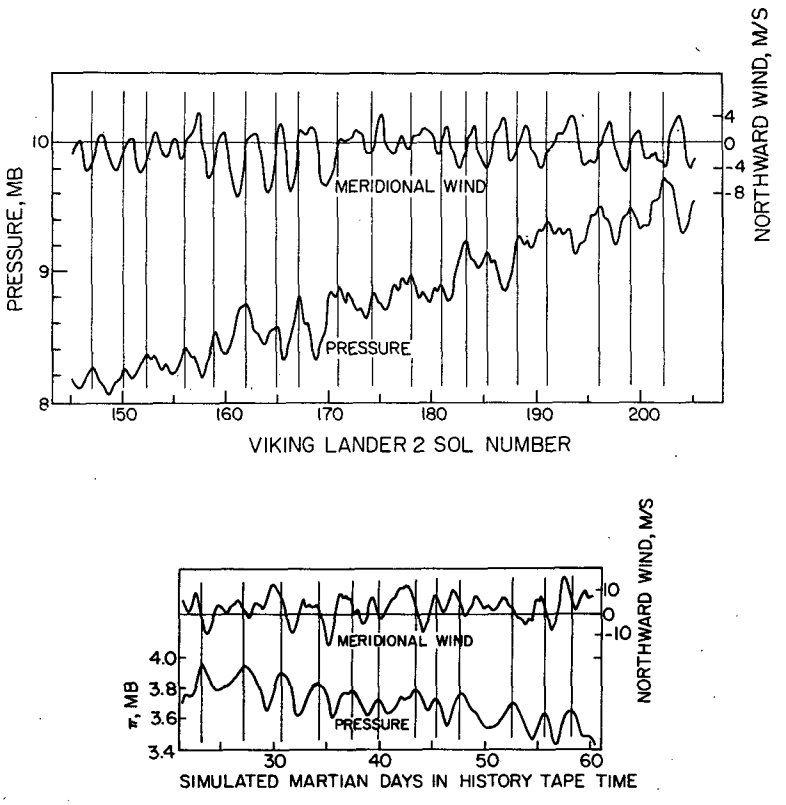

FIG. 22. Comparison of Viking observations of surface pressures and winds (Lander 2: 48°N, 225°W, northern midwinter, upper panel) with surface pressures and winds generated by the model (50°S, 120°W, southern midwinter, lower panel). The wind observations are at a height of 1.6 m; the model results apply at $\sigma = 0.89$ (~0.8 km, see Fig. 1). A rough comparison can be obtained by multiplying the model winds by a boundary layer scaling factor 0.4.

zonal wind in the lower part of the atmosphere. This characteristic, along with the vertical westward phase tilt and the patterns of heat and momentum fluxes, is what is expected of baroclinic waves of the type first analyzed theoretically by Charney (1947) and Eady (1949). As Fig. 21 shows, the wavenumber of these disturbances is about 4–6. In the vicinity of Hellas (45°S, 290°W), there is an intense transient low which moves eastward at first, then appears to regenerate farther west while a portion of the disturbance continues eastward as a rapidly decaying trough (upper panels, sol 56 hour 12 and sol 57 hour 0). This behavior is reminiscent of the behavior of terrestrial traveling waves as they move through the large-amplitude terrestrial standing wave troughs. The weak disturbance near 90°W also appears to be strongly influenced by topography as it crosses the eastern slope of the Tharsis ridge.

The model simulated transient waves can be compared with Viking observations. Fig. 22 shows a time series of pressure and surface wind at the Viking 2 lander site (48°N) during northern winter ($L_s \approx 250°$) compared with a time series of the surface pressure and meridional wind at $\sigma = 0.89$ from the simulation. Both time series have had diurnal variations removed by application of a 1-sol running mean. The similarity between the two time series is evident. Both show fairly regular pressure oscillations with a predominant period of about 3 sols, and coherent fluctuations of wind and pressure such that falling pressure is correlated with poleward wind, as it is for eastward-traveling waves. The periodicity in pressure appears as a highly significant 3.1-sol spectral peak in the Viking lander 2 observations over a period of more than 100 sols (Ryan *et al.*, 1979; Tillman *et al.*, 1979). The amplitudes of the observed and simulated pressure variations are comparable, with an rms of ~5% of the mean pressure in both cases. The observed 3.1-sol waves have been inferred to have a zonal wavenumber of about 4 and a phase speed ~13 m s^{-1} (Leovy, 1979; Barnes, 1980). This wavenumber and phase speed agree very well with the corresponding values in the simulation.

The simulation also produces transient waves in the tropics and summer hemisphere. These are primarily the thermally-driven diurnal tides. The spectra shown in Fig. 23 illustrate this. Aside from

considerable red noise, the most prominent feature is the spectral peak in the upper level meridional wind. The amplitude is larger on the equator than at 40°N, and, at both latitudes, the amplitude is greater over upland (120°W) than over lowland (210°W). By integration of this feature over frequency, after subtracting an estimated background noise, we infer a diurnal wind amplitude at 0°N, 120°W, of ~5 m s^{-1}. The longitudinal variation, corresponding to a modulation of the westward-propagating tide as it moves over the upland regions, is evident in individual wind maps. Although we did not expect to obtain many components of the thermally-driven tides at all adequately with a model that has such severe vertical truncation, the simulated tides are in fair agreement, insofar as they can be compared, with those observed by Viking during the relatively clear midsummer conditions (Hess *et al.*, 1977), as well as with the tides derived by Zurek (1976) with his "clear atmosphere" models. To the extent that the trapped external diurnal modes dominate the tidal structure, the model may correctly simulate the tidal characteristics, especially the surface pressure and wind.

The contributions of the transient waves to the energy conversions are also shown schematically in Fig. 20 (the dotted line arrows). In the winter (southern) hemisphere, these waves transport heat poleward and upward, and they transport eastward momentum, on the average, toward the most baroclinically active zone just poleward of the zonal jet. Thus they convert ZAPE to EAPE, EAPE to EKE, and EKE to ZKE, in the manner of classical baroclinic waves. The transient eddy contribution to the total energy cycle in the summer (northern) hemisphere is relatively small, but there is a tendency for these eddies, which are primarily just the diurnal tide, to transport heat down the meridional temperature gradient and upward, (Figs. 10 and 13), and to transport eastward momentum toward the eastward wind maximum (Fig. 16).

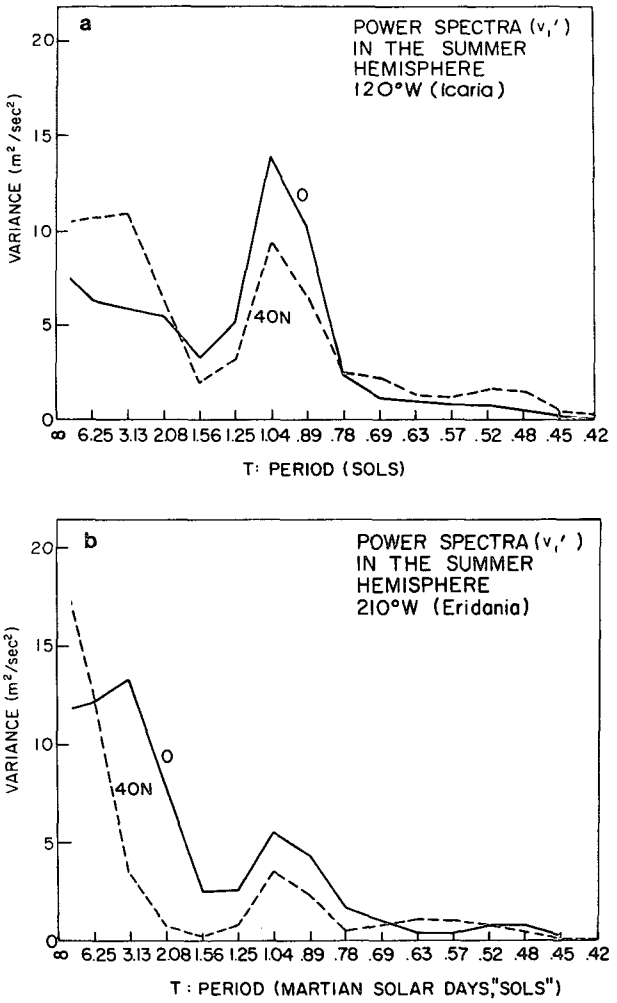

FIG. 23. Power spectra of meridional wind at level 1 (v') at 120°W and at 210°W, illustrating the diurnal tide.

4. Concluding remarks

Comparisons between this simulation, the simulation using the model of *I*, the terrestrial atmospheric circulation, and available Martian observations provide some insights into Martian atmospheric processes.

First, comparing this simulation with the results from *I*, we find that the zonally-averaged properties of the atmosphere are insensitive to the specific structure of the model and to the inclusion of the large-amplitude topography. The meridional temperature gradient, the static stability, and the rate of condensation of CO_2 in the winter polar cap are very similar. The zonal and meridional winds have about the same character, although weaker in the equatorial zone in the current calculation, but this is mainly due to the smaller solar flux received by Mars during southern winter compared with northern winter. On the other hand, the large-amplitude topography produces prominent standing waves within the eastward wind belts of both hemispheres, but in both simulations the total eddy kinetic energy is about the same as the kinetic energy of the zonally-averaged flow. In both calculations, the transient eddies of the winter hemisphere are mainly eastward-propagating baroclinic waves, of about wavenumber 4, while those of the tropics and summer hemisphere are mainly westward-propagating diurnal tides.

Comparing the simulation with the earth's atmosphere, we find that the model's winter hemisphere circulation is similar in many respects to winter circulation on the earth. The locations of zonal westward and eastward winds at the surface

TABLE A1. Band model parameters.

Weak bands*

Wavelength (μm)	a	b	g_0 (cm^{-1})	q_s
1.316	0.393	0.599	5.04×10^{-2}	0.397
1.455	0.402	0.547	4.35×10^{-2}	0.434
1.600	0.376	0.607	2.81×10^{-2}	0.391

Strong bands*

Wavelength (μm)	a	b	f_0	d_0 (cm^{-1})	q_f	q_d
2.020	0.445	0.711	1.51×10^{-3}	1.16×10^{2}	−0.060	0.496
2.759	0.396	0.668	6.83×10^{-2}	6.01×10^{1}	−0.215	0.509
4.301	0.551	0.745	1.06	2.40×10^{1}	0.444	0.211
14.93	0.323	0.566	1.53×10^{-1}	5.44×10^{1}	−0.256	0.879

* The parameters given in this table for weak and strong bands are used in Eqs. (A1) and (A2) with E, W and P having units of cm^{-1}, cm-atm, and mb, respectively. Allowance has been made for the larger self broadening of CO_2 than the amount of pressure broadening by N_2.

and aloft are very similar, although the calculation for Mars produces a stronger eastward mean jet stream. The qualitative differences in the summer wind distributions seem to be a straightforward consequence of the absence of Martian oceans. Baroclinic waves develop in the region of strong poleward temperature gradient, as in the earth's atmosphere, but the wavenumber is somewhat smaller and the waves are more regular in the Mars simulation. This may be a consequence of the much larger static stability which develops in the winter subpolar region of the model. The Mars simulation shows topographically-forced waves of two kinds: mechanically-forced waves in winter in the region of eastward flow, and thermally-forced waves in summer, also with maximum amplitude in the region of eastward flow. These are analogous to the quasi-stationary Rossby waves which are topographically-forced in the terrestrial winter midlatitudes, and the thermally-forced continental plateau circulations which form in summer in the subtropical latitudes on earth. The mechanical forcing of the winter waves in the Martian simulation produces a conversion of eddy kinetic energy to eddy available potential energy, and a conversion of eddy available potential energy to zonal available potential energy which is not as clearly evident on earth.

The mean meridional circulation dominates in the transports of heat and momentum in the Martian atmosphere at high latitudes as well as low latitudes. This is mainly a consequence of the condensation flow, a uniquely Martian atmospheric process, but the simulation also generates overturning meridional circulations that are stronger than those observed on earth. We do not think that this is a model-dependent result. The momentum and heat balance requirements can be satisfied with a more intense zonally symmetric circulation on Mars because of the stronger thermal forcing (Held and Hou, 1980).

Where comparisons can be made between the model results and observations of the Martian atmosphere, the agreement is good. The meridional temperature gradient as a function of latitude and height, and the large static stability and high-level temperature maximum near the edge of the condensing CO_2 polar cap are observed features which are reproduced by the model. The rate of condensation of CO_2 in the winter cap and the equatorward boundary of the condensing cap which are produced by the model are also in general agreement with the observations, although the very precise agreement found may be fortuitous. We conclude, however, that the polar cap heat balance is radiatively controlled and that in the absence of heavy dust loading, atmospheric heat transport plays a minor role in the polar cap heat balance.

The baroclinic waves generated by the model have periods, wavelengths, amplitudes, and phase-speeds which are in close agreement with those of the waves measured during winter at the Viking 2 site, and we therefore infer that the observed waves also arise from baroclinic instability. The regular nature of the calculated and observed Martian baroclinic waves is somewhat similar to what is seen in some rotating tank experiments, particularly the one of Fultz and Spence (1977), in which steady wave regimes and regularly vacillating wave regimes are produced in a cylindrical tank without a central core. The experimental feature which was required to obtain these regimes was a large static stability in the upper part of the fluid. We have seen that this is a characteristic of both the simulated and observed Martian temperature fields at midlatitudes during winter. The very large static stability near the edge of the winter polar cap, as well as the strong radiative damping may particularly favor such a regime.

We are unable to make observational comparisons of the stationary waves generated by the model. That could be done with observations from a low polar orbiter which carried an atmospheric thermal sounder, or from a network of observing stations on the surface.

The principal discrepancy between the simulation and observations is the much lower static stability of the tropics and summer hemisphere. This makes the dynamically active region of strong horizontal temperature gradients only about ⅔ as deep in the model calculations as on the true planet. This is undoubtedly a direct consequence of our neglect of dust heating in the model.

Acknowledgment. We are very grateful to Warren Van Camp and Donald Weidmann for their help with

TABLE A2. Values for sundry parameters.

Name	Symbol	Value	Comments
CO_2 band parameter	$\bar{c}$	0.606	see Eq. (A4)
CO_2 band parameter	$\bar{q}$	0.405	*ibid.*
Latent heat of CO_2	L	5.9×10^5 J kg^{-1}	
Gas constant for CO_2	R	189 J kg-K^{-1}	
Acceleration of gravity	g	3.72 m s^{-2}	
Specific heat at constant pressure	c_p	736 J kg-K^{-1}	
Average temperature	$\bar{T}$	200 K	see footnote to Table A3
Thermal diffusivity	κ_a	7.70×10^{-4} m^2 s^{-1}	*ibid.*
Thermal inertia parameter	I	270 J (m^2-S$^{1/2}$-K)$^{-1}$	$(\rho ck)^{1/2}$ where ρ, c and k are soil density, heat capacity and thermal conductivity
Critical Richardson number	Ri_c	1	Eq. (A17)
Richardson number adjustment time scale	τ_R	2×10^4 s	Eq. (A17)
Time scale for smoothing subsurface temperature	t_{smooth}	0.2 sol	
Tropopause pressure	p_T	1 mb	
Visual optical depth of polar hood	τ_v	1	
Mean radius of particles in the polar hood	$\bar{r}$	2×10^{-6} m	
Scattering asymmetry parameter	2β	0.164	see Eq. (A8)
Radius of Mars	a	3.393×10^6 m	
CO_2 ice albedo	A_{ice}	0.6	

the calculations, to James Cutts for providing albedo information, and to Robert Haberle for helpful discussions of the diabatic and frictional algorithms. This research was supported in part by grants from the NASA Planetary Programs Office, Atmospheric Sciences Division.

APPENDIX

Details of Heating and Friction Algorithms

The equivalent widths of the near IR and 15 μm bands of CO_2, $E_i(w,p,T)$, were represented empirically as functions of absorber path length w (atmos-cm), pressure p (mb), and temperature T (K), by one of the following formulas:

$$E_i(w,p,T) = g_0(T/T_0)^{q_s} w^b p^a, \qquad \text{(A1)}$$

appropriate for the weaker bands, or

$$E_i(w,p,T) = d_0(T/T_0)^{q_d} \ln[1 + f_0(T/T_0)^{q_f} w^b p^a], \qquad \text{(A2)}$$

appropriate for the stronger bands, by fitting the parameters a and b and either g_0, and q_s or d_0, q_d, f_0, and q_f to the data of Howard *et al.* (1955)[6] and Burch *et al.* (1962).[7] The resulting parameter values are given in Table A1. The fractional amount of solar energy absorbed by CO_2 above the level at which the pressure is p_b, $S(p_b)$, can be written

$$S(p_b) = \sum_{i=1}^{n} E_i F_i / F_{\mathrm{tot}}, \qquad \text{(A3)}$$

where F_i is the incident solar irradiance in band i, and F_{tot} the total incident solar irradiance. In applying this formula, the Curtis Godson approximation was used to replace the pressure in (A1) or (A2) (i.e., p was set equal to $p_b/2$, and the pressure-weighted mean temperature $\bar{T}$ replaced temperature). The near IR bands were combined into a single effective band by setting $q_d = 0$, introducing an average temperature coefficient $\bar{q}$ for q_f, an average value of $b/(a + b) = \bar{c}$, and linearizing about a standard temperature $T_1 = 200$ K. S was then a function of a single parameter, i.e.,

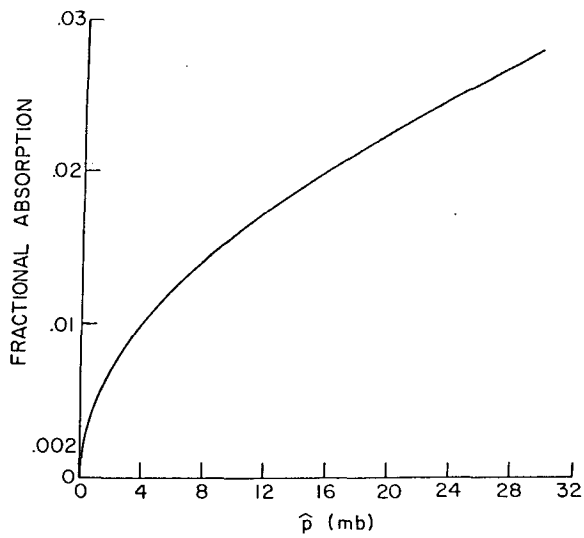

FIG. A1. Dependence of fractional solar absorption S on scaled pressure $\hat{p}$.

[6] Howard, J., D. Burch and D. Williams, 1955: Near-infrared transmission through synthetic atmospheres. Air Force Cambridge Research Laboratory, Rep. 55-213, 244 pp. [NTIS AD-087679].

[7] Burch, D. E., D. Gryvnak, E. B. Singleton, W. L. France and D. Williams, 1962: Infrared absorption by carbon dioxide, water vapor, and minor atmospheric constituents. Air Force Cambridge Research Laboratory, Rep. 62-698, 316 pp. [NTIS AD-287406].

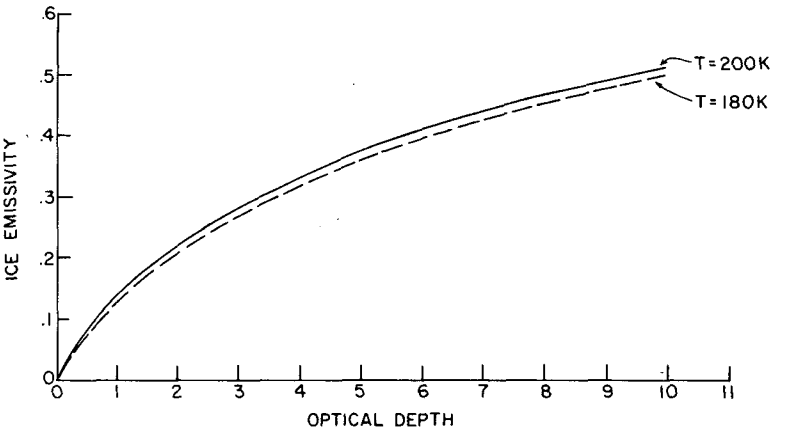

FIG. A2. Dependence of ice cloud emissivity e on ice cloud visible optical thickness.

$$\hat{p} \equiv p_b\left[1 + \bar{q}\left(\frac{T - T_1}{T_1}\right)\right]\Big/(2\mu)^{\bar{c}}, \qquad \text{(A4)}$$

where μ is the cosine of the solar zenith angle. Values of $\bar{q}$ and $\bar{c}$ are included in Table A2; Fig. A1 illustrates the dependence of S on $\hat{p}$. Solar heating of each layer was obtained by differencing the fluxes at the layer boundaries. The solar flux at the ground, F_s in Eq. (3) of the text, was evaluated by applying Eq. (A3) at the lower boundary.

In order to evaluate the contributions of the 15 μm band radiation to net heating and to $F^{\downarrow}_{IR}$, the 15 μm band contribution to downward flux at pressure level p was evaluated from

$$F^{\downarrow}_{CO_2}(p) = 2\pi\left\{B(T_T)E^*_{trop} - \int_{B_p}^{B_{trop}} E^*dB + B(T_T)[E^*_{top} - E^*_{trop}]\right\}, \qquad \text{(A5)}$$

where B is the Planck Function at the center of the 15 μm band, E^* is the equivalent width for diffuse radiation with E^*_{trop} being the value corresponding to the path between the tropopause and pressure level p, and E^*_{top} the value for the path between the top of the atmosphere and pressure level p. In (A5) it has been assumed that the stratosphere is isothermal at temperature T_T. Similarly, the 15 μm band upward flux at p is

$$F^{\uparrow}_{CO_2}(p) = 2\pi\left\{B(T_6)E^*_s - \int_{B_p}^{B_{A,S}} E^*dB + B(T_G)[\Delta\nu/2 - E^*_s]\right\}, \qquad \text{(A6)}$$

where T_6 is the extrapolated surface atmospheric temperature, E^*_s applies to the path between the ground and pressure level p, and $\Delta\nu$ is the effective CO_2 band width. Note that the value of $\Delta\nu$ does not contribute directly to $F^{\downarrow}_{IR}$ or to heating, however. E^* was evaluated using (A2), the 15 μm band parameters in Table A1, and the approximation

$$E^* \equiv \int_0^1 \mu E(\mu)d\mu \approx \bar{\mu}E(\bar{\mu}), \qquad \text{(A7)}$$

with $\bar{\mu}$ set equal to 0.488, a value obtained by optimizing the approximation (A7) in comparison with numerical integrations over μ. The integrals in (A5) and (A6) were approximated by

$$\int E^*dB = \sum E^*_j \Delta B_j,$$

where E^*_j corresponds to the path between the midpoint of layer j and pressure level p, and ΔB_j is the difference between the Planck functions corresponding to temperatures at the boundaries of layer j. Evaluation of these temperatures is described below.

The contribution of ice clouds to thermal infrared flux was evaluated using an ice-cloud emissivity

$$e(T) = \int_0^1\int \frac{B_\nu(T)[1 - \exp(-\tau_\nu v/\mu)]d\nu\mu d\mu}{\sigma T^4/2\pi}, \qquad \text{(A8)}$$

where

$$v \equiv (1 - \bar{\omega}_0)^{1/2}(1 - \bar{\omega}_0 + 2\beta\bar{\omega}_0)^{1/2}$$

is the optical depth scaling factor from the two-stream approximation (Sagan and Pollack, 1967), expressed in terms of single scattering albedo $\bar{\omega}_0$, and asymmetry parameter 2β. These quantities, and the infrared optical depth τ_ν were evaluated as described in the text assuming optical depth of the cloud in the visible equaled 1.0, a value estimated from the visual appearance of surface features through polar hood clouds, and brightness variations associated with the clouds (Briggs and Leovy, 1974). The numerator of (A8) was evaluated over the entire

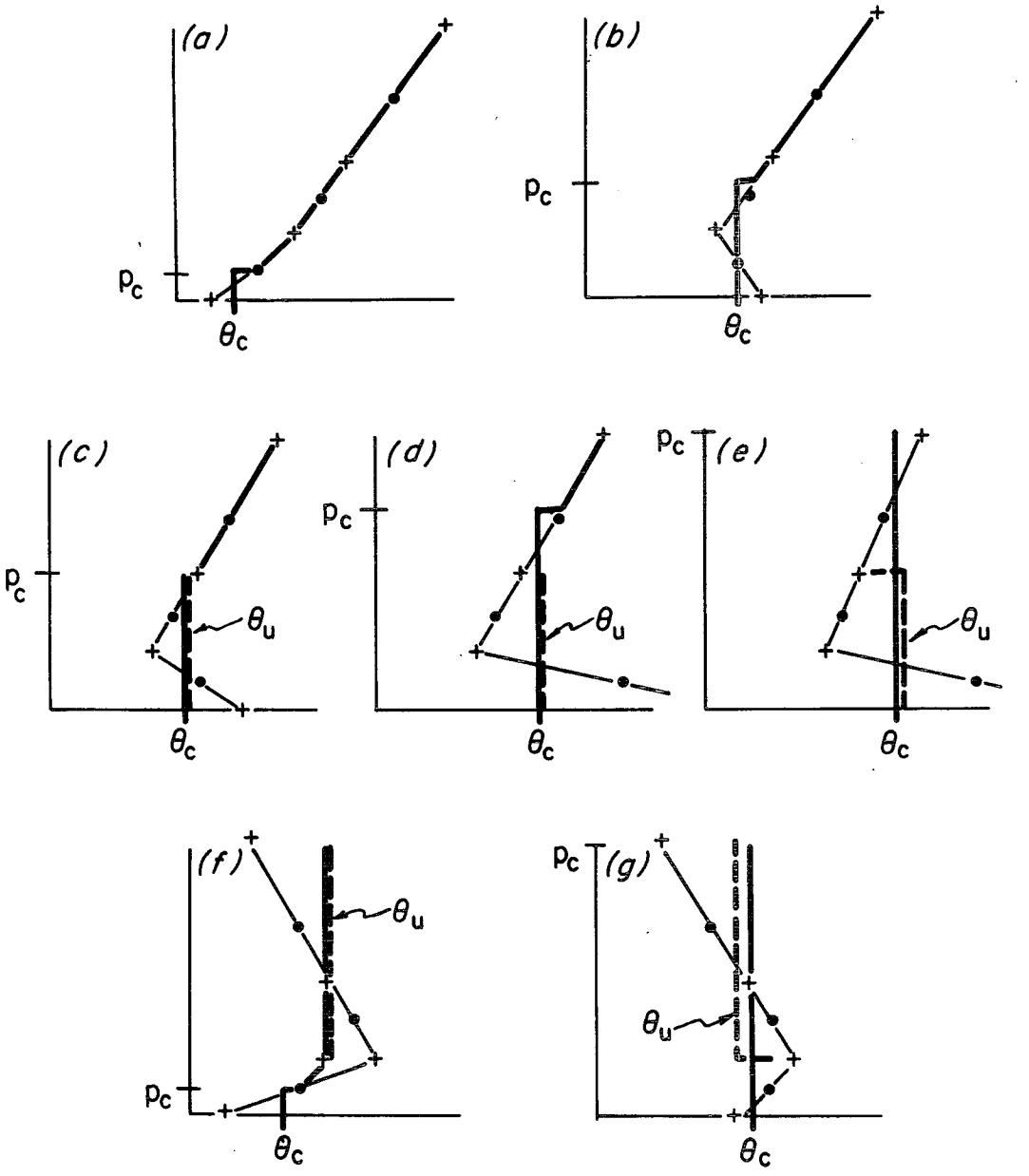

FIG. A3. Examples illustrating convective layer modeling. Symbols (●) indicate layer mean values of θ, (+) indicate interpolated or extrapolated values.

infrared spectrum exclusive of the 15 μm band (480–860 cm^{-1}). Fig. A2 shows $e(T)$ versus visible optical depth. The emissivity curve for 180 K was used, and emissivity averaged ~0.13 for the entire column. The ice cloud contributions to upward and downward fluxes were evaluated from the summations over layers

$$F^{\downarrow}_{\text{ice}}(p) = \sum_j e_j \sigma T_j^4, \tag{A9}$$

$$F^{\uparrow}_{\text{ice}}(p) = \sum_j e_j \sigma T_j^4 - \sigma T_g^4 \sum_j e_j. \tag{A10}$$

Eqs. (A4), (A5), (A9), and (A10) were used to evaluate the net infrared fluxes at the interfaces between layers, at the surface, and at the top of the atmosphere ($p = 0$). These were differenced and divided by the layer masses to obtain the thermal infrared contribution to net layer heating, and (A4) and (A9) evaluated at $p = p_s$ were used to obtain $F^{\downarrow}_{\text{IR}}$ in Eq. (2) of the text. Note that the upper layer for this radiative calculation as well as for the solar absorption includes both the upper model layer and the dynamically inert "stratosphere."

For both the radiative and convective calcula-

TABLE A3. Values of the heat exchange (c_h) and friction (c_f) coefficients for unstable boundary layers.

Bulk Richardson number			Bulk Richardson number		
Lower bound	Upper bound	c_h	Lower bound	Upper bound	c_f
0	2×10^{-3}	1/35	0	2×10^{-3}	1/45
2×10^{-3}	2×10^{-1}	1/30	2×10^{-3}	1	1/40
2×10^{-1}	5	1/25	1	10	1/35
5	50	1/20	10	80	1/30
50	300	1/16	80	800	1/25
300	—	$\max\{1/13, \tilde{w}/c_f w_s\}$*	800	—	1/20

* The factor $(\tilde{w}/c_f w_s)$ is a value appropriate under conditions of free convection, where $\tilde{w}$, the free convection "velocity," equals $0.2(\kappa_a g/\bar{T})^{1/3}(T_G - \theta_c)^{1/3}$. The parameters w_s, κ_a, g, $\bar{T}$, T_G and θ_c refer to the magnitude of the wind at the midpoint of the bottom layer of the model; thermal diffusivity of the air at the Martian surface; acceleration of gravity; average temperature; instantaneous ground temperature; and potential temperature of the PBL, respectively.

tions, it was necessary to have temperature values at the layer boundaries, including the tropopause and the surface. For the two internal boundaries (levels 2 and 4, see Fig. 1) and the tropopause, potential temperature was assumed to vary linearly in log pressure between the interface between the two lowest layers and the tropopause, with the variation specified by the potential temperatures evaluated from the two upper layer mean temperatures and pressures. The surface atmospheric temperature was then obtained by linear extrapolation of the potential temperature evaluated as described above at the interface between the two lowest layers and potential temperature at the midpoint of the lowest layer. This procedure emphasized variations in temperature near the ground.

In order to describe the convective heating algorithm, let θ_1, θ_3 and θ_5 be the potential temperatures of the three layers, and θ_0, θ_2, θ_4 and θ_6 be the potential temperatures of the tropopause, the two internal interfaces, and the atmosphere at the surface, respectively. The atmosphere was first convectively adjusted, with the potential temperature of the adjusted pair or triplet of layers designated θ_u. In the case of an unstable surface layer ($T_G > T_6$), a convective layer was assumed to exist with potential temperature θ_c and top pressure p_c, with θ_c the convectively adjusted potential temperature of the lowest layer. Pressure p_c was then determined by the following rules: (i) if $\theta_c < \theta_5$, $p_c = p_5$, and $\theta_c = (\theta_5 + \theta_6)/2$; (ii) if $\theta_4 \leq \theta_c < \theta_2$, p_c was determined by upward extrapolation of θ_c into the middle layer in such a way as to leave the internal energy content of that layer unchanged; (iii) if $\theta_1 > \theta_c > \theta_2$, p_c was determined by upward extrapolation of θ_c into the top model level in such a way as to leave the internal energy content of that layer unchanged; (iv) if $\theta_c > \theta_1$, $p_c = p_T$. Convective adjustment and the determination of p_c and θ_c are illustrated in Fig. A3. Note that this procedure allowed only the value of $p_c = p_5$ for case (i), but because the lower layer was sufficiently thin, this was not a severe drawback.

The surface stress and heat flux were evaluated as follows. The magnitude of the surface stress was given by

$$\tau = \rho_s u_*^2, \tag{A11}$$

where ρ_s was surface atmospheric density, and

$$u_* = c_f w_s \tag{A12}$$

for wind speed w_s of the lowest layer. Table A3 gives values of c_f used for unstable conditions, expressed in terms of the boundary-layer bulk Richardson number,

$$\mathrm{Ri}_B = R(\theta_c - T_G)\ln(P_s/p_c)/w_s^2,$$

where R is the gas constant for CO_2. For stable cases, the prescription

$$c_f(\text{stable}) = \begin{cases} c_0 \equiv 1/45, & 0.0 \leq \mathrm{Ri}_B \leq 0.05 \\ c_0[1 + c_0(20\ \mathrm{Ri}_B - 1)]^{-1}, & \mathrm{Ri}_B > 0.05. \end{cases} \tag{A13}$$

The surface heat flux was given by

$$F_{\text{conv}} = -c_p \rho_s u_* c_h(\theta_c - T_G), \tag{A14}$$

where c_p is the heat capacity at constant pressure. For unstable conditions, values given in Table A3 were used for $c_h(\mathrm{Ri}_B)$. For stable conditions, c_h was simply set equal to $1.28c_f$.

Richardson number adjustment between two layers (say layers 3 and 5) was governed by the Richardson number

$$\mathrm{Ri}_{3,5} = R\ln(p_5/p_3)\frac{(\tilde{\omega}_3 + \tilde{\omega}_5)}{2}\frac{(\theta_3 - \theta_5)}{|\mathbf{v}_3 - \mathbf{v}_5|^2}, \tag{A15}$$

where $\mathbf{v}_i$ is the ith layer wind, and $\tilde{\omega}_i$ is the factor used to convert potential temperature to temperature in the ith layer ($\tilde{\omega}_i = [p_i/p_s]^\kappa$, $\kappa \equiv R/c_p$). When $\mathrm{Ri}_{3,5} < 1$ and $\theta_3 \geq \theta_5$ the following replacement formulas were used:

$$\left.\begin{aligned} \mathbf{v}_3' &= \mathbf{v}_3 + \Delta\mathbf{v}M_5/M_3 \\ \mathbf{v}_5' &= \mathbf{v}_5 - \Delta\mathbf{v} \end{aligned}\right\}, \tag{A16}$$

where

$$\Delta\mathbf{v} = \frac{\Delta t}{\tau_R}[1 - (\mathrm{Ri}_{3,5}/\mathrm{Ri}_c)^{1/2}] \times [1 + M_5/M_3]^{-1}[\mathbf{v}_5 - \mathbf{v}_3]. \tag{A17}$$

Here Δt was the time step, $\tau_R = 2 \times 10^4$ the adjustment time, $\mathrm{Ri}_c = 1.0$ the critical Richardson num-

ber, and M_3 and M_5 were the masses per unit area of the layers. When $\theta_3 < \theta_5$,

$$\Delta \mathbf{v} = M_3(\mathbf{v}_5 - \mathbf{v}_3)/(M_3 + M_5). \qquad \text{(A18)}$$

Table A2 lists the additional input parameters used in the simulation.

REFERENCES

Barnes, J., 1980: Time spectral analysis of midlatitude disturbances in the Martian atmosphere. *J. Atmos. Sci.*, **37**, 2002–2015.

Blackmon, M., J. M. Wallace, N.-C. Lau and S. L. Mullen, 1977: An observational study of the Northern Hemisphere wintertime circulation. *J. Atmos. Sci.*, **34**, 1040–1053.

Briggs, G., 1974: The nature of the residual Martian polar caps. *Icarus*, **23**, 167–191.

——, and C. Leovy, 1974: Mariner 9 observations of Mars' north polar hood. *Bull. Amer. Meteor. Soc.*, **55**, 278–296.

——, W. A. Baum and J. Barnes, 1979: Viking orbiter imaging observations of dust in the Martian atmosphere. *J. Geophys. Res.*, **84**, 2795–2820.

Charney, J., 1947: The dynamics of long waves in a baroclinic westerly current. *J. Meteor.*, **4**, 135–162.

Conrath, B., 1975: Thermal structure of the Martian atmosphere during dissipation of the dust storm of 1971. *Icarus*, **24**, 36–46.

——, R. Curran, R. Hanel, V. Kunde, W. Maguire, J. Pearl, J. Pirraglia, J. Welker and T. Burke, 1973: Atmospheric and surface properties of Mars obtained by infrared spectroscopy on Mariner 9. *J. Geophys. Res.*, **78**, 4267–4278.

Curran, R. J., B. J. Conrath, R. A. Hanel, V. G. Kunde and J. C. Pearl, 1973: Mars: Mariner 9 spectroscopic evidence for H_2O clouds. *Science*, **182**, 381–383.

Deardorff, J. W., 1972: Parameterization of the planetary boundary layer for use in general circulation models. *Mon. Wea. Rev.*, **100**, 93–106.

Ditteon, R., and H. H. Kieffer, 1979: Optical properties of solid CO_2: applications to Mars. *J. Geophys. Res.*, **84**, 8294–8301.

Eady, E. T., 1949: Long waves and cyclone waves. *Tellus*, **1**, 33–52.

Eliassen, A., and E. Palm, 1960: On the transfer of energy in stationary mountain waves. *Geofys. Publ.*, **22**, 1–23.

Fultz, D., and T. W. Spence, 1977: Experiments on wave-transition spectra and vacillation in an open rotating cylinder. *J. Atmos. Sci.*, **34**, 1261–1285.

Gierasch, P. J., and R. M. Goody, 1968: A study of the thermal and dynamical structure of the Martian lower atmosphere. *Planet. Space Sci.*, **16**, 615–646.

Halem, M., J. Shukla, Y. Mintz, M. L. Wu, R. Godbole, G. Herman, Y. Sud, 1979: Comparisons of observed seasonal climatic features with a winter and summer numerical simulation produced with the GLAS general circulation model. Report of the JOC Study Conference on Climate Models: Performance, Intercomparison and Sensitivity Studies, GARP Publ. No. 22, Vol. I, WMO/ICSU, Geneva, 207–253.

Hanel, R., B. Conrath, W. Hovis, V. Kunde, P. Lowman, W. Maguire, J. Pearl, J. Pirraglia, C. Prabhakara, B. Schlachman, G. Levin, P. Straat and T. Burke, 1972: Investigation of the Martian environment by infrared spectroscopy on Mariner 9. *Icarus*, **17**, 423–442.

Held, I. M., 1975: Momentum transport by quasi-geostrophic eddies. *J. Atmos. Sci.*, **32**, 1494–1497.

——, and A. Y. Hou, 1980: Nonlinear axially symmetric circulations in a nearly inviscid atmosphere. *J. Atmos. Sci.*, **37**, 515–533.

Hess, S. L., R. M. Henry, C. B. Leovy, J. A. Ryan and J. E. Tillman, 1977: Meteorological results from the surface of Mars: Viking 1 and 2. *J. Geophys. Res.*, **82**, 4559–4574.

Irvine, W. M., and J. B. Pollack, 1968: Infrared properties of water and ice spheres. *Icarus*, **8**, 324–360.

——, T. Simon, D. H. Menzel, C. Pikoos and A. T. Young, 1968: Multicolor photoelectric photometry of the brighter planets, part III, observations from Boyden Observatory. *Astron. J.*, **73**, 807–828.

Kieffer, H. H., S. C. Chase, Jr., E. Miner, G. Munch and G. Neugebauer, 1973: Preliminary report on infrared radiometric measurements from the Mariner 9 spacecraft. *J. Geophys. Res.*, **78**, 4291–4312.

Kliore, A. J., G. Fjeldbo, B. Seidel, M. J. Sykes and P. M. Woiceshyn, 1973: S-band occultation measurements of the atmosphere and topography of Mars with Mariner 9: Extended mission coverage of polar and intermediate latitudes. *J. Geophys. Res.*, **78**, 4331–4351.

Kuhn, W. R., S. K. Atreya and S. E. Postawko, 1979: The influence of ozone on Martian atmospheric temperature. *J. Geophys. Res.*, **84**, 8341–8342.

Leighton, R. B., and B. C. Murray, 1966: Behavior of carbon dioxide and other volatiles on Mars. *Science*, **153**, 136–144.

Leovy, C. B., 1979: Martian meteorology. *Annual Review of Astronomy and Astrophysics*, Vol. 17, Annual Reviews, Inc., 387–411.

——, and Y. Mintz, 1969: Numerical simulation of the weather and climate of Mars. *J. Atmos. Sci.*, **26**, 1167–1190.

Lorenz, E., 1955: Available potential energy and the maintenance of the general circulation. *Tellus*, **7**, 157–167.

Mass, C., and C. Sagan, 1976: A numerical circulation model with topography for the Martian summer hemisphere. *J. Atmos. Sci.*, **33**, 1418–1430.

Owen, T., and K. Biemann, 1976: Composition of the atmosphere at the surface of Mars: detection of Argon-36 and preliminary analyses. *Science*, **193**, 801–803.

Pollack, J. B., C. B. Leovy, Y. Mintz and W. Van Camp, 1976: Winds on Mars during the Viking season: predictions based on a general circulation model with topography. *Geophys. Res. Lett.*, **3**, 479–483.

——, D. S. Colburn, F. M. Flasar, R. Kahn, C. E. Carlston and D. Pidek, 1979: Properties and effects of dust particles suspended in the Martian atmosphere. *J. Geophys. Res.*, **84**, 2929–2946.

——, ——, R. Kahn, J. Hunter, W. Van Camp, C. E. Carlston and M. R. Wolfe, 1977: Properties of aerosols in the Martian atmosphere, as inferred from Viking lander imaging data. *J. Geophys. Res.*, **82**, 4479–4496.

Ryan, J. A., S. L. Hess, R. M. Henry, C. B. Leovy and J. E. Tillman, 1978: Mars meteorology: three seasons at the surface. *Geophys. Res. Lett.*, **5**, 715–718.

Sagan, C., and J. B. Pollack, 1967: Anisotropic, nonconservative scattering and the clouds of Venus. *J. Geophys. Res.*, **72**, 469–477.

Slipher, E. C., 1962: *The Photographic Story of Mars*. Sky Publishing Corp., Cambridge, 168 pp.

Somerville, R. C. J., P. H. Stone, M. Halem, J. E. Hansen, J. S. Hogan, L. M. Druyan, G. Russell, A. A. Lacis, W. J. Quirk and J. Tenenbaum, 1974: The GISS model of the global atmosphere. *J. Atmos. Sci.*, **31**, 84–117.

Stone, P. H., S. Chow and W. J. Quirk, 1977: The July climate and a comparison of the January and July climates simulated by the GISS general circulation model. *Mon. Wea. Rev.*, **105**, 170–194.

Tillman, J. E., R. M. Henry and S. L. Hess, 1979: Frontal systems during passage of the Martian north polar low over Viking lander 2 site prior to the first 1977 global dust storm. *J. Geophys. Res.*, **84**, 2947–2955.

Webster, P. J., 1977: The low latitude circulation of Mars. *Icarus*, **30**, 626–649.

Zurek, R. W., 1976: Diurnal tide in the Martian atmosphere. *J. Atmos. Sci.*, **33**, 321–337.